

ISSN 1732-9353 (suspended)
eISSN 2543-7496

Scientific Review

Engineering and Environmental Sciences

Przegląd Naukowy
Inżynieria i Kształtowanie Środowiska

Vol. 31 (4)

2022
Quarterly

Issue 98

SCIENTIFIC REVIEW
ENGINEERING AND ENVIRONMENTAL SCIENCES
Quarterly

EDITORIAL BOARD

Kazimierz Adamowski (University of Ottawa, Canada), **Kazimierz Banasik – Chairman** (Warsaw University of Life Sciences – SGGW, Poland), Andrzej Ciepeliowski (Warsaw University of Life Sciences – SGGW, Poland), Tomáš Dostál (Czech Technical University in Prague, Czech Republic), Vidmantas Gurlkys (Aleksandras Stulgniskis University, Kaunas, Lithuania), Małgorzata Gutry-Korycka (University of Warsaw, Poland), Zbigniew Heidrich (Warsaw University of Technology, Poland), Silvia Kohnova (Slovak University of Technology, Bratislava, Slovak Republic), Andrzej J. Kosicki (Maryland State Highway Administration, Baltimore, USA), Hyosang Lee (Chungbuk National University, Korea), Athanasios Loukas (University of Thessaly, Volos, Greece), Jurík Luboš (Slovak Agriculture University, Nitra, Slovak Republic), Viktor Moshynskiy (National University of Water Management and Nature Resources Use, Rivne, Ukraine), Magdalena Daria Vaverková (Mendel University in Brno, Czech Republic)

EDITORIAL OFFICE

Tomasz Gnatowski (Deputy-chairman), Weronika Kowalik, Paweł Marcinkowski (Editorial Assistant Environmental Sciences), Katarzyna Pawluk, **Mieczysław Poloński (Chairman)**, Magdalena Daria Vaverková, Grzegorz Wierzbicki, Grzegorz Wrześniński (Editorial Assistant Engineering Sciences)

REVIEWERS Vol. 31

Vytautas Akstinas, Ahmed Alalikhani, Munaf Al-Ramahee, Muna Al-Rubaye, Ali Yasar Ameer, Libor Ansoerge, Ir Antonius, Jerzy Bobiński, Casey D. Bray, Agnieszka Bus, Lenka Demková, Marek Dohojda, Zlata Dolaček-Alduk, Eslam Elhawary, Kazimierz Furtak, Orlando Garcia-Rodríguez, Marek Gielczewski, Andrzej Głuchowski, Tomasz Gnatowski, Piotr Iwicki, Małgorzata Jastrzębska, Piotr Jaśkowski, Katarzyna Jeleniewicz, Luboš Jurík, Michał Juszczyk, Marek Kalenik, Agnieszka Karczmarczyk, Adam Kiczko, Marta Kiraga, Vasyl M. Korbutiak, Adam Koziół, Agnieszka Leśniak, Mateusz Malinowski, Ivan Marovič, Mariusz Maślak, Magdalena Michel, Vu Minh Phap, Mohamed Khatif Tawaf bin Mohamed Yusof, Muthana Muhaisin, Erfan Najaf, Sobia Naseem, Katarzyna Osińska-Skotak, Anna Ostańska, Katarzyna Pactwa, Michal Petru, Kazimierz Piekut, Konrad Podawca, Piotr Prochoń, Abdulmir H. Qasim, Elżbieta Radziszewska-Zielina, Lidia Reczek, Lada Stejskalová, Mateusz Stelmaszczyk, Jan Szatyłowicz, Bartosz Szeląg, Olga Szlachetka, Małgorzata Sztubecka, Barbara Tomczyk, Roman Trach, Andrzej Truty, Viktor Tur, Robert Ulewicz, Eva Vitková, Ivanna Voronkova, Stanisław Wierzbicki, Elżbieta Wołejko, Piotr Woyciechowski, Ali asar Yasar Ameer

EDITORIAL OFFICE ADDRESS

Wydział Budownictwa i Inżynierii Środowiska SGGW, ul. Nowoursynowska 159, 02-776 Warsaw, Poland
tel. (+48 22) 59 35 363, 59 35 210, 59 35 302
e-mail: srees@sggw.edu.pl
<https://srees.sggw.edu.pl>

ISSN 1732-9353 (suspended)
e-ISSN 2543-7496

Electronic version of the Scientific Review Engineering and Environmental Sciences is primary version

All papers are indexed in the data bases as follows: AGRO(Poznań), BazTech, Biblioteka Nauki, **CrossRef**, **DOAJ**, **Google Scholar**, **Index Copernicus**, INFONA, POL-Index, **SCOPUS**, SIGŻ(CBR)

Scientific Review

Engineering and Environmental Sciences

Przegląd Naukowy
Inżynieria i Kształtowanie Środowiska

Vol. 31 (4)

2022

Issue 98

Contents

DUHAIM H.M., MASHREI M.A. Stress–strain relationship of ductile materials and flexural behavior of ductile over-reinforced concrete beams	225
SAHIB H.A., Al-ASADI A.K. Prediction of shear strength of CFRP-strengthened reinforced recycled aggregate concrete beams using various strengthening methods	238
HUSSEIN O.A., ABBAS A.N. Self-compacting concrete strengthening efficiency investigation using recycled steel waste as fibres	249
DAWOOD M.H., Al-ASADI A.K. Mechanical properties and flexural behaviour of reinforced concrete beams containing recycled concrete aggregate	259
GAJDÁČ I., KUČERA L., GAJDOŠÍK T., KONSTANTOVA V. A review of the factors and input parameters influencing the range of an Edison electric vehicle according to measurements	270
CIĘŻKOWSKI W., FRAK M., KARDEL I., KOŚCIELNY M., CHORMAŃSKI J. Long-term water quality monitoring using Sentinel-2 data, Głuszyńskie Lake case study	283

Wydawnictwo SGGW, Warsaw 2022



Wydawnictwo SGGW



wydawnictwosggw

Editorial work – Anna Dołomisiewicz, Violetta Kaska, Tomasz Ruchniewicz

ISSN 1732-9353 (suspended) eISSN 2543-7496

Hussein M. DUHAIM

Mohammed A. MASHREI ✉  <https://orcid.org/0000-0002-5909-756X>

University of Thi-Qar, College of Engineering, Iraq

STRESS–STRAIN RELATIONSHIP OF DUCTILE MATERIALS AND FLEXURAL BEHAVIOR OF DUCTILE OVER-REINFORCED CONCRETE BEAMS

Key words: ductile materials, SFRC, SIFCON, UHPFRC, over-reinforced beam, flexural behavior, ductility

Introduction

According to ACI 318 (American Concrete Institute [ACI], 2014) and based on the reinforcement ratio, the flexural reinforced concrete beams can be classified to balanced reinforced, under-reinforced, and over-reinforced sections. When the tensile reinforcement ratio is less than the balance reinforcement ratio, the under-reinforced failure occurs by the yielding of steel before the crushing of concrete. This mode of failure is characterized by significant deflection and wide cracks. Balanced failure occurs by the yielding of steel in tension and crushing of concrete in the compression zone at the same

time. However, the over-reinforced failure occurs suddenly by crushing of concrete in the compression zone before yielding of steel reinforcement in tension zone with little deflection and few cracks.

To avoid the brittle compression failure, many codes limit the use of over-reinforced sections (Ziara, Haldane & Hood, 2000; Siddiqi, 2016). However, a high tensile reinforcement ratio is often used to decrease the size of the beam and to provide adequate stiffness (Whitehead & Ibell, 2004; Ahmed, Farghal, Nagah & Haridy, 2007; Ali & Tarkhan, 2015; Mohamed, 2018; Deng, Zhang, Ma, Li & Sun, 2021). By reducing the beam's size, the formwork dimensions reduce and save time, material, and labor during construction. Furthermore, reducing the beam's size boosts the structure's efficiency by providing more rentable space. In recent years, the construction industry that requires the use of over-

-reinforced sections in large projects, such as high-rise buildings and bridges has been employed (Ali & Tarkhan, 2015).

To change the failure mode of concrete from brittle to ductile failure for over-reinforced concrete beams, there are different techniques used in previous studies to improve the ductility of concrete in the compression zone, such as using a steel plate bolted with a compression zone of concrete (Alasadi, Shafiqh & Ibrahim, 2020), addition confinement in the compression zone (Priastiw, Imran, Nuroji & Hidayat, 2014; Tee, Al-Sanjery & Chiang, 2017), a block or precast block can be cast in compression zone (Liu & Wu, 2007; Wu, 2008), and using ductile materials, this can do by replacing the concrete in the compression zone with a layer of material that has both high strength and ductility.

A few studies have been carried out to use ductile materials in the compression zone. Thus, this paper aimed to study the effect of using ductile materials in compression zone on the flexural performance of over-reinforced concrete beams as well as to study the mechanical properties of the materials. The ductile materials used in this study were steel fiber reinforced concrete (SFRC), slurry infiltrated fiber concrete (SIFCON), and ultra-high performance fiber reinforced concrete (UHPC). To achieve the goal of the study, four composite beams were cast and tested to investigate the flexural capacity, failure modes, crack patterns, load-deflection relationships, ductility index, and toughness.

Background

Steel fiber reinforced concrete (SFRC)

This type of FRC is made of cement, fine and coarse aggregates, water, and steel fibers that are actually randomly distributed in the

concrete. The purpose of randomly distributed discontinuous steel fibers is to bridge across the cracks that formed inside concrete to provide ductility after cracking through the pullout resistance of steel fibers (Kobayashi, 1976). The SFRC has a higher strain capacity than normal concrete (NC), making it ideal for usage in members that are subjected to large plastic deformation demands. Also, SFRC has durability and serviceability more than NC (Germano, Plizzari & Tiberti, 2013). The FRC has many applications, such as applications in ground slabs, precast members, and shotcrete tunnel linings (Orouji, Zahrai & Najaf, 2021).

Slurry infiltrated fiber concrete (SIFCON)

This type of concrete is different from traditional FRC in respect of composition and fabrication. The fiber content in FRC usually ranges from 1 to 3% by volume, whereas fiber content in SIFCON typically ranges from 5 to 20% by volume (Balaji & Thirugnanam, 2018).

The SIFCON matrix has a high cement content. It may contain fine or coarse sand, as well as mineral and chemical admixture, but no coarse aggregates. Therefore, the SIFCON matrix is either cement paste or flowing cement mortar as opposed to the traditional FRC (Salih, Frayyeh & Ali, 2018). Also, SIFCON production differs from FRC, in SIFCON fibers are placed in a casting mold, and then a slurry of cement is infiltrated over the rich fiber layers. Fibers are placed in the mold by hand or with the use of fiber-dispersing units (Shelorkar, 2021). Vibration is often required to achieve proper slurry infiltration of the fiber bed (Khamees, Kadhum & Alwash, 2020). While in FRC, fibers are added to the dry or wet concrete mix.

Ultra-high performance fiber reinforced concrete (UHPRFC)

This type of concrete is a cementitious composite with a high cement content, small aggregate size, and binder (pozzolana, fly ash, silica fume, reactive powder) as well as a low water to cement ratio.

Because of the low water to cement ratio, UHPC mixes are characterized by low workability. One method to improve the workability of UHPC is using a super-plasticizer. Furthermore, using silica fume in UHPC can fill spaces between coarser particles due to its smaller size and spherical form, so enhancing the strength properties via pozzolanic reactions. Despite enhancing the stiffness and strength, the failure mode of plain UHPC is very brittle; therefore, post-cracking behavior is limited (Qadir, Faraj, Sherwani, Mohammed & Younis, 2020). Fibers can change the failure mode of plain UHPC from brittle to ductile mode and increase the tensile strength, toughness, and deformation ability of the resultant composite, the name of this type of concrete is UHPRFC (Khalil & Tayfur, 2013).

Experimental program

Materials preparation

All materials used were conformed to the requirement of the American Association State Highway and Transportation (ASTM) standards. The NC mix consists of cement, sand, gravel, and water in addition to a super-plasticizer. The SFRC mix differs from the NC mix by containing steel fibers. The UHPRFC and SIFCON mix consist of cement, quartz sand, water, super-plasticizer, and steel fibers. Furthermore, mineral

admixtures such as silica fume are used as a partial replacement (10%) of cement weight in the UHPRFC mix.

The materials used throughout the work are Portland cement 42.5 grade, natural sand as fine aggregate with a maximum size of 4.75 mm, crushed coarse aggregate (gravel) with a maximum nominal size of 14 mm, high-performance super-plasticizer concrete admixture, densified silica fume with grading below 1 μm , and quartz sand with small grading 0.3–0.7 mm to ensure complete infiltration of the slurry over the dense steel fiber (Abeer, Dawood & Ghalib, 2020). Finally, hooked-end steel fiber with volume fractions of 1.5, 1.5 and 7.5% were used in the SFRC, UHPRFC, and SIFCON mixes, which has a length of 30 mm and diameter of 0.5 mm with an aspect ratio (l/d) of 60 and ultimate tensile strength of 1,200 MPa based on the manufacturer company requirements.

Compressive strength and stress–strain relationship

The uniaxial compressive strength of NC and ductile materials was determined by the compressive test of cylinder specimens of size 100 \times 200 mm. Cylinder specimens for each material were cast from the same batch of beams. The stress–strain relationship and crack pattern of NC and ductile materials under the uniaxial compressive test are shown in Figure 1.

As depicted in Figure 1, the presence of hooked-end steel fiber (V_f 1.5%) with NC increased the strain capacity of concrete from 0.0032 to 0.0080 as well as increased compressive stress, which means the ductility and toughness of SFRC were higher than those of NC. The UHPRFC and SIFCON showed high strength and strain

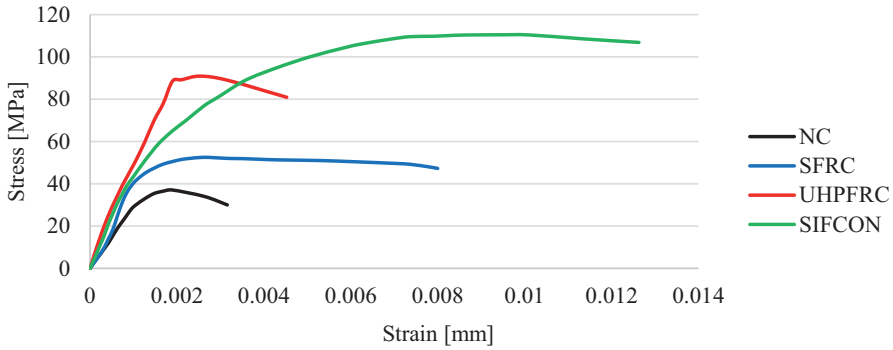


FIGURE 1. Uniaxial compression stress–strain relationships for different concrete types

capacity when compared to NC. Noting that despite using the same V_f 1.5% of steel fiber, UHPFRC exhibited strain capacity less than SFRC, which was 0.0045. This may be related to the fact that the behavior of UHPC is more brittle, which led to reduced deformation ability in comparison to SFRC. While SIFCON exhibited strain capacity greater than other types of FRC, which was 0.01263. This is attrib-

uted to the high content of steel fibers in SIFCON, which led to increased deformation ability.

Details of reinforcement

Figure 2 shows details of the over-reinforced beam. Based on the cross-section assumption, the critical thickness of partial replacement of NC with ductile materials

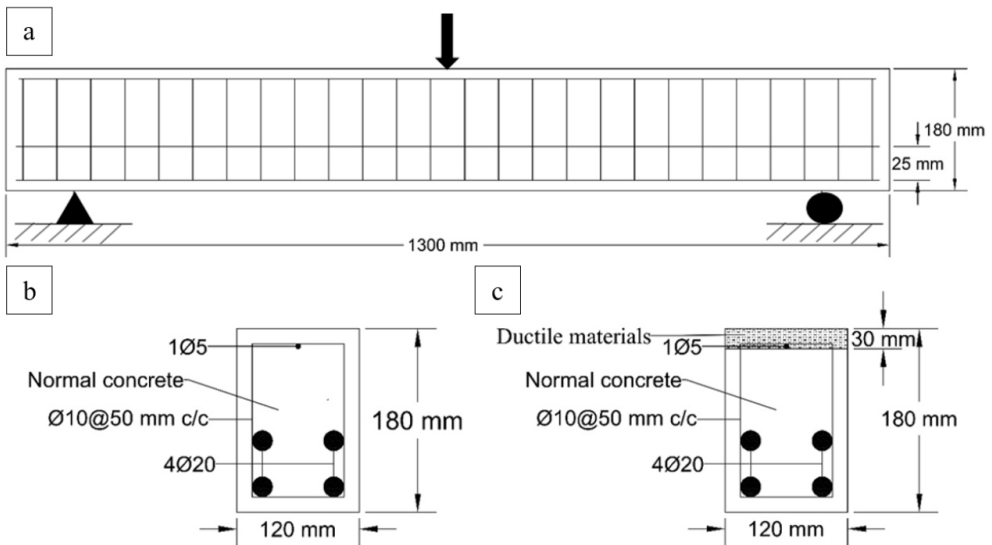


FIGURE 2. Details of reinforcement and cross-section of over reinforced concrete beams: (a) beam reinforcement; (b) cross section of reference beam; (c) cross section of composite beams

layer in the compression zone was around 30 mm (more than 10% of the beam depth), based on findings by Deng, Ma, Ye and Li (2021).

Table 1 illustrates the mechanical properties of deformed steel rebars that conformed to the requirements of ASTM A615/A615M (American Association State Highway and Transportation [ASTM], 2015).

Each beam has a tensile reinforcement ratio of 8.548%. It is more than the balancing limit which is 1.988% according to ACI 318 (ACI, 2014), in order to

obtain heavily reinforced beams and to ensure the mode of failure is compression failure.

Mix proportions

Based on trial mixes for various proportions of constituents in order to determine the required strength, the final mix proportions of NC, SFRC, UHPFRC, and SIFCON slurry are presented in Table 2. The workability was checked as the control test for the fresh concrete properties, as shown in Figure 3.

TABLE 1. Mechanical properties of deformed steel rebars

Bar diameter [mm]	Yield strength (Y_s) [MPa]	Tensile strength (T_s) [MPa]	T_s/Y_s [-]	Total elongation [%]	Bending test pass/fail
10	618	773	1.25	10.00	pass
20	599	713	1.19	13.50	pass

TABLE 2. Mix proportions of NC, SFRC, UHPFRC, and SIFCON slurry for 1 m³ of concrete

Concrete type	Cement [kg]	Silica fume [kg]	Sand [kg]	Quartz sand [kg]	Coarse aggregate [kg]	w/c or w/b ratio	Steel fiber [%]	Super-plasticizer [%]
NC	410	–	750	–	1 100	0.45	–	0.4
SFRC	410	–	750	–	1 100	0.45	1.5	0.4
UHPFRC	900	90	–	990	–	0.19	1.5	1.8
SIFCON	850	–	–	850	–	0.31	7.5	1.6



FIGURE 3. Trail mix and fresh concrete test

Casting and curing

The casting of the beams in this study contains four over-reinforced concrete beams, three of them were composite beams created by using NC and one layer of ductile materials (SFRC, UHPFRC, and SIFCON) in the compression zone, while the last beam was cast with NC only to use as a reference beam. The casting of the ductile materials layer in the compression side was immediately after casting the NC to increase the bond strength between different concrete parts. Each part was compacted using an electric vibrating table to ensure removing the entrapped air and increasing the bond between parts, allowing them to behave as one part. After casting all specimens, it was covered with plastic sheets and demolded at the age of two days and all specimens were immersed in water until testing.

Endurance test

After curing, the over-reinforced concrete beams were tested up to failure under three-point loading with a clear span of 1,100 mm. Figure 4 shows the test setup and instrumentation that were used to monitor the beams during the testing.

Test results and discussion

Crack pattern and modes of failure

The first crack in NC beam was flexural type and initiated at the early stage of loading in the tension zone. With increasing load, a few cracks with small width were formed and propagated in their length toward the compression zone. When the load approximately reached its maximum capacity, the number and width of final cracks were comparatively small, the cover of concrete in the compression zone began to collapse, and concrete crushing failure occurred. This type of failure is a brittle compression failure without sufficient warning before failure.

For other beams that had ductile materials layer (SFRC, UHPFRC, and SIFCON) in the compression zone, their experimental phenomenon was similar to that of the NC at the initial stage of loading. As the load approximately reached its maximum capacity, the cracks extended toward the compression zone and widened rapidly. Also, the flexural crack length and deflection at midspan significantly increased with the increase of load as compared to the NC beam. Finally, the beam failed by crushing of ductile materials layer in the compression zone. The

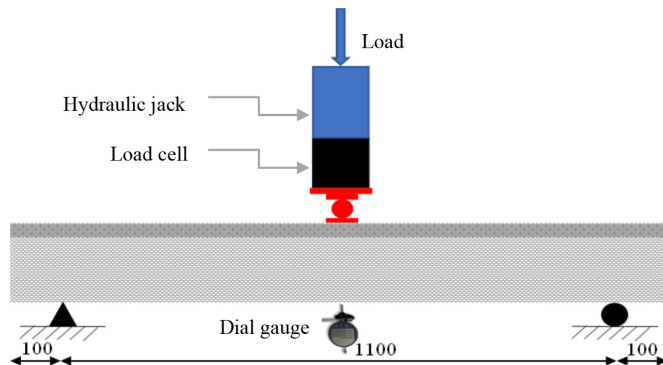


FIGURE 4. Details of the test setup (all dimensions in mm)

modes of failure of composite beams stayed flexural compression failure, but these beams have ductile behavior. Therefore, the use of the ductile materials layer at the compression zone changed the failure mode of over-reinforced concrete beams from brittle to ductile failure and led to an increase in their load-carrying capacity.

Although the ultimate load carried by the SIFCON beam is higher than the other beams, the SIFCON layer maintained the beam's integrity. This can be attributed to the high content of steel fibers in the SIFCON layer compared to SFRC and UHPFRC layers. Also, it should be mentioned that despite using the same volume fraction of steel fibers (1.5%) for UHPFRC and SFRC layers, the deformation ability of the SFRC beam was more than the UHPFRC beam. This may be due to the presence of steel fibers, which led to an increase the contact between the particles of aggregates when the cracks formed, and this is may not found in the UHPFRC beam.

The crack pattern and failure modes of all tested beams are shown in Figure 5. No debonding between NC and ductile materials layers in the composite beams even at the failure state has been observed.

This can be attributed to the fact that good bond strength is achieved between the surfaces of the ductile material and NC, in

addition to the presence of stirrups in beams that work as effective shear connectors (Atta & Khalil, 2016).

Load deflection relationships

To investigate the effect of using ductile materials on improving the flexural performance of over-reinforced concrete beams used in this study, the relation of applied load versus deflections at mid-span for all beams are plotted in Figure 6 to show their structural behavior, flexural capacity, deformation ability of beams, ductility, and toughness.

All over-reinforced concrete beams exhibited flexural compression failure noting that the failure of the composite beams was through the crushing of the concrete after an obvious large deflection compared to the reference beam. Therefore, the composite beams exhibited load–deflection behavior more ductile than that of the reference beam under the same load conditions because using ductile materials leads to an increase in both load-carrying capacity and ductility. However, the curve of UHPFRC rapidly drops after reaching peak load and then continues to deform up to failure. Figure 6 shows that the using a layer of SFRC, UHPFRC, or SIFCON in the compression zone gives higher deflection at failure than that of NC by 133.70, 55.84 and 81.92%, respectively,

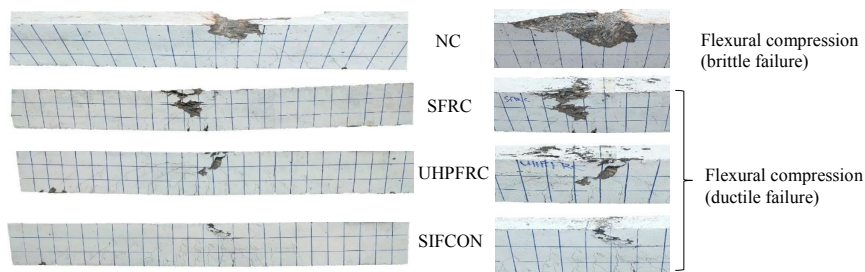


FIGURE 5. Crack pattern and failure modes of over-reinforced concrete beams

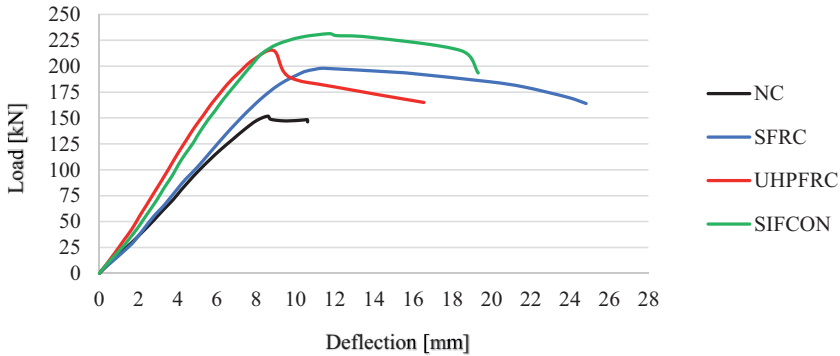


FIGURE 6. Load deflection relationships for over-reinforced beams

and enhances load-carrying capacity by 30.45, 41.65 and 52.46%, respectively. Noting that the increases in load-carrying capacity of UHPFRC and SIFCON beams were more than the SFRC beam. This may be due to the high compressive strength and the different production of UHPFRC and SIFCON compared to SFRC, where the high fiber content in SIFCON led to the strong bond between steel fibers and matrix interfaces. In contrast, the increase in deflection at failure for the SFRC beam was greater than that of UHPFRC and SIFCON beams. This may be related to increasing the contact between the particles of aggregates when the cracks form due to the presence of steel fibers as compared to the UHPFRC beam without coarse aggregate in the UHPFRC layer. Therefore, it is possible that if using steel fibers content greater than 1.5% in the UHPFRC mix, the

ductility results of beams would have been better, which needs to be investigated further in future studies. While in the case of SIFCON beams, the lack of ductility compared to SFRC beam may be attributed to using a strengthening layer with a small thickness, so it needs to be investigated using SIFCON in the compression zone with a layer thickness greater than 30 mm in future studies.

Flexural capacity

As shown in Table 3, the ultimate loads of composite beams containing a layer of SFRC, UHPFRC, and SIFCON in the compression zone improved by 30.45, 41.65 and 52.46%, while the corresponding deflections improved by 33.30, 3.61 and 36.44%, respectively, compared to those of NC beam.

TABLE 3. Experimental results of all beams

Beam type		Ultimate load [kN]	Ultimate deflection [mm]	Mode of failure
Reference beam	NC	151.78	8.59	flexural compression (brittle)
Composite beam	SFRC	198.00	11.45	flexural compression (ductile)
	UHPFRC	215.00	8.90	flexural compression (ductile)
	SIFCON	231.40	11.72	flexural compression (ductile)

The improvement in the ultimate load and the corresponding deflection is attributed to the significant effect of the high compressive strength and high ultimate compressive strain capacity of ductile materials, respectively, compared to those of NC that was used in the reference beam. These results indicate that using ductile materials in the compression zone of concrete has a considerable effect on improving the flexural capacity of over-reinforced beams.

Ductility

The ability of any material or member to experience plastic deformation and energy absorption is measured by its ductility, which also refers to the ability of the material or member to resist applied loads after yielding without critical failure. There are many forms of ductility, such as curvature, rotational, and deflection ductility (Deng et al., 2018). The definition of deflection ductility is investigated in this study. As defined by Pam, Kwan and Islam (2001), the deflection ductility index ($\mu\Delta$) is the ratio of maximum deflection (Δ_{\max}) to yield deflection (Δ_y). Several various definitions have been suggested by Park (Park, 1989) to estimate yield and maximum deflections. The definition adopted here for yield deflection is

by using the secant stiffness method at 75% of the ultimate load (P_u), while the definition of maximum deflection is related to how the failure point is defined. The most realistic definition of maximum deflection is when the load-carrying capacity has undergone a small reduction after ultimate load or when the material fractures, whichever occurs first. For more details, see reference (Park, 1989). Noting that the reduction in load-carrying capacity after ultimate load was adopted by 15%, according to reference (Pam et al., 2001). Figure 7 shows the definition of yield and maximum deflections.

In order to reveal the effect of ductile materials layers on ductility, the ductility index ratio (R) is calculated, which is the ratio of the deflection ductility index of the composite beam to that of the corresponding reference beam. The obtained main results of loads and the deflection ductility indexes with the ductility index ratio for the tested beams are presented in Table 4. It emerged that the use of ductile materials layer (SFRC, UHPFRC, and SIFCON) in the compression zone of over-reinforced concrete beams showed a considerable increase in ductility as compared to that of the reference beam.

Based on the above, composite beam with SFRC or SIFCON layer exhibited

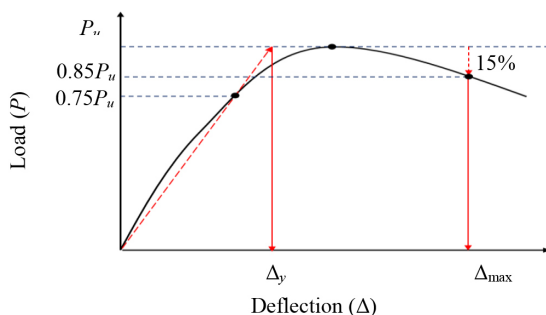


FIGURE 7. Definition of yield and maximum deflections

TABLE 4. The deflection ductility indexes and the ductility index ratio of tested beams

Beam type		Δ_y [mm]	Δ_{max} [mm]	$\mu\Delta$ [-]	R [%]
Reference beam	NC	7.68	10.60	1.38	–
Composite beam	SFRC	9.50	24.20	2.55	84.78
	UHPRFC	7.50	11.25	1.50	8.70
	SIFCON	8.75	19.25	2.20	59.42

better performance than that with the UHPRFC layer in deflection ductility. This may be related to the fact that the behavior of UHPC is brittle. Generally, the use of hooked-end steel fiber ($V_f 1.5\%$) with NC increased the ductility of concrete by 84.78%. Finally, the ductility of the over-reinforced concrete beams has been improved using ductile materials in the compression zone.

Toughness

Toughness (U_t) is defined as the material's ability to absorb energy before failure. However, it is attached to combining both strength and ductility in a single measurable property and requires a delicate balance of strength and ductility (Abeer et al., 2020). The material must be strong and ductile in order to be tough. A strong material but has limited ductility as brittle material is not tough, and similarly, highly ductile material but has low strength is not tough. The material must be able to sustain high stresses as well as high strains to be considered tough. Flexure toughness is related to the area under the stress–strain or load–deflection curves and calculated using Equation (1).

$$U_t = \text{area under the load } (P) \text{ curve} - \text{deflection } (\Delta) \text{ curve} = P \times \Delta \quad (1)$$

The toughness results of the tested beams are shown in Table 5. It emerged that the toughness of composite beams showed an acceptable increment when compared to the reference beam, which was 279.93, 146.05 and 235.13% for SFRC, UHPRFC, and SIFCON, respectively. This behavior may be explained by the fact that the ability of steel fibers to bridge across the cracks led to an increase in the ultimate load and deflection, which resulted in an increase in the area under the load–deflection curve.

TABLE 5. The toughness values of tested beams

Beam type		Toughness [N·m ⁻¹]	The increment in toughness over NC beam [%]
Reference beam	NC	996.18	–
Composite beam	SFRC	3 784.81	279.93
	UHPRFC	2 451.15	146.05
	SIFCON	3 338.55	235.13

Table 5 shows that the composite beam with SFRC exhibits a higher increment in toughness. In general, it can be concluded that the use of ductile materials in the compression zone of composite beams provides an improvement in the energy absorption and ductility for over-reinforced concrete beams.

Conclusions

Based on the results obtained in the current study, the following conclusions can be drawn:

- Using ductile materials layer in the compression zone of over-reinforced beams changed the failure mode from brittle compression failure to ductile flexural compression failure.
- Using ductile materials layers in the compression zone of over-reinforced concrete beams with tensile reinforcement ratio of 8.548% increased load-carrying capacity and deformation ability at failure by up to 52.46 and 133.70%, respectively.
- The load-carrying capacity of composite beams containing a layer of SFRC, UHPFRC, and SIFCON in the compression zone improved by 30.45, 41.65 and 52.46%, while the corresponding deflections improved by 33.30, 3.61 and 36.44%, respectively, compared to NC beam.
- The increase in ductility by using SFRC, UHPFRC, and SIFCON layers in the compression zone was 84.78, 8.70 and 59.42%, respectively, while the increase in toughness was 279.93, 146.05 and 235.13%, respectively.
- Finally, it can be stated that the acceptable compressive strength and high deformation ability of SFRC have the potential to enable economical and ductility together compared with UHPFRC and SIFCON.

References

Abeer, S. Z., Dawood, M. B. & Ghalib, M. H. (2020). Flexural behavior of continuous beams consisting of normal concrete and SIFCON under static and repeated loads. *IOP Conference Series: Materials Science*

and Engineering, 870 (1), 1–14. <https://doi.org/10.1088/1757-899X/870/1/012113>

- Ahmed, M. M., Farghal, O. A., Nagah, A. K. & Haridy, A. A. (2007). Effect of confining method on the ductility of over-reinforced concrete beams. *Journal of Engineering Sciences*, 35 (3), 617–633. <https://doi.org/10.21608/JESAUN.2007.112873>
- Alasadi, S., Shafiqh, P. & Ibrahim, Z. (2020). Experimental study on the flexural behavior of over reinforced concrete beams bolted with compression steel plate: Part I. *Applied Sciences (Switzerland)*, 10 (3), 1–20. <https://doi.org/10.3390/app10030822>
- Ali, A. M. & Tarkhan, M. A. (2015). Experimental investigation of confining the compression zone in over-reinforced beams. *International Journal of Engineering Sciences and Research Technology*, 4 (11), 611–617.
- American Association State Highway and Transportation [ASTM] (2015). *Standard specification for deformed and plain carbon-steel bars for concrete reinforcement* (ASTM A615/A615M). Washington: American Association State Highway and Transportation.
- American Concrete Institute [ACI] (2014). *Building code requirements for structural concrete* (ACI 318). Farmington Hills: American Concrete Institute.
- Atta, A. M. & Khalil, A. E. H. (2016). Improving the failure mode of over-reinforced concrete beams using strain-hardening cementitious composites. *Journal of Performance of Constructed Facilities*, 30 (5), 04016003. [https://doi.org/10.1061/\(ASCE\)CF.1943-5509.0000857](https://doi.org/10.1061/(ASCE)CF.1943-5509.0000857)
- Balaji, S. & Thirugnanam, G. S. (2018). Behaviour of reinforced concrete beams with SIFCON at various locations in the beam. *KSCCE Journal of Civil Engineering*, 22 (1), 161–166. <https://doi.org/10.1007/s12205-017-0498-9>
- Deng, M., Ma, F., Ye, W. & Li, F. (2018). Flexural behavior of reinforced concrete beams strengthened by HDC and RPC. *Construction and Building Materials*, 188, 995–1006. <https://doi.org/10.1016/j.conbuildmat.2018.08.124>

- Deng, M., Zhang, M., Ma, F., Li, F. & Sun, H. (2021). Flexural strengthening of over-reinforced concrete beams with highly ductile fiber-reinforced concrete layer. *Engineering Structures*, 231, 111725. <https://doi.org/10.1016/j.engstruct.2020.111725>
- Germano, F., Plizzari, G. A. & Tiberti, G. (2013). Experimental study on the behavior of SFRC columns under seismic loads. In J. G. M. Van Mier, G. Ruiz, C. Andrade, R. C. Yu & X. X. Zhang (Eds). *Proceedings of the 8th International Conference on Fracture Mechanics of Concrete and Concrete Structures, FraMCoS-8* (pp. 1171–1182). Barcelona: Cimne.
- Khalil, W. I. & Tayfur, Y. R. (2013). Flexural strength of fibrous ultra high performance reinforced concrete beams. *ARPN Journal of Engineering and Applied Sciences*, 8 (3), 200–214.
- Khamees, S. S., Kadhum, M. M. & Alwash, N. A. (2020). Effects of steel fibers geometry on the mechanical properties of SIFCON concrete. *Civil Engineering Journal (Iran)*, 6 (1), 21–33. <https://doi.org/10.28991/cej-2020-03091450>
- Kobayashi, K. (1976). Steel Fiber Reinforced Concrete. *Zairyo/Journal of the Society of Materials Science, Japan*, 25 (277), 937–945. <https://doi.org/10.2472/jms.25.937>
- Liu, K. & Wu, Y. F. (2007). Compression yielding by sifcon block for FRP-reinforced concrete beams. *Proceedings of the 1st Asia-Pacific Conference on FRP in Structures*, 1, 411–416.
- Mohamed, H. A. (2018). Improvement in the ductility of over-reinforced NSC and HSC beams by confining the compression zone. *Structures*, 16 (2), 129–136. <https://doi.org/10.1016/j.istruc.2018.09.005>
- Orouji, M., Zahrai, S. M. & Najaf, E. (2021). Effect of glass powder & polypropylene fibers on compressive and flexural strengths, toughness and ductility of concrete: an environmental approach. *Structures*, 33, 4616–4628. <https://doi.org/10.1016/j.istruc.2021.07.048>
- Pam, H. J., Kwan, A. K. H. & Islam, M. S. (2001). Flexural strength and ductility of reinforced normal- and high-strength concrete beams. *Proceedings of the Institution of Civil Engineers: Structures and Buildings*, 146 (4), 381–389. <https://doi.org/10.1680/stbu.2001.146.4.381>
- Park, R. (1989). Evaluation of ductility of structures and structural assemblages from laboratory testing. *Bulletin of the New Zealand Society for Earthquake Engineering*, 22 (3), 155–166. <https://doi.org/10.5459/bnzsee.22.3.155-166>
- Priastiwati, Y. A., Imran, I., Nuroji & Hidayat, A. (2014). Behavior of ductile beam with addition confinement in compression zone. *Procedia Engineering*, 95, 132–138. <https://doi.org/10.1016/j.proeng.2014.12.172>
- Qadir, H. H., Faraj, R. H., Sherwani, A. F. H., Mohammed, B. H. & Younis, K. H. (2020). Mechanical properties and fracture parameters of ultra high performance steel fiber reinforced concrete composites made with extremely low water per binder ratios. *SN Applied Sciences*, 2(9), 1594. <https://doi.org/10.1007/s42452-020-03425-3>
- Salih, S., Frayyeh, Q. & Ali, M. (2018). Fresh and some mechanical properties of sifcon containing silica fume. *MATEC Web of Conferences*, 162, 1–7. <https://doi.org/10.1051/mateconf/201816202003>
- Shelorkar, A. P. (2021). Slurry Infiltrated Fibrous Concrete (SIFCON) – a review. *International Journal of Research Publication and Reviews*, 2 (8), 780–787.
- Siddiqi, Z. A. (2016). *Concrete Structures*. Part 1 (3rd ed.). Lahore: Help Civil Engineering Publisher.
- Tee, H. H., Al-Sanjery, K. & Chiang, J. C. L. (2017). Behaviour of reinforced concrete beams with confined concrete related to ultimate bending and shear strength. *AIP Conference Proceedings*, 1, 020060. <https://doi.org/10.1063/1.4976924>
- Whitehead, P. A. & Ibell, T. J. (2004). Deformability and ductility in over-reinforced concrete structures. *Magazine of Concrete Research*, 56 (3), 167–177. <https://doi.org/10.1680/MACR.2004.56.3.167>
- Wu, Y. F. (2008). Ductility demand of compression yielding fiber-reinforced polymer-reinforced concrete beams. *ACI Structural Journal*, 105 (1), 104–110. <https://doi.org/10.14359/19074>

Ziara, M. M., Haldane, D. & Hood, S. (2000). Proposed changes to flexural design in BS 8110 to allow over-reinforced sections to fail in a ductile manner. *Magazine of Concrete Research*, 52 (6), 443–454. <https://doi.org/10.1680/MACR.2000.52.6.443>

Summary

Stress–strain relationship of ductile materials and flexural behavior of ductile over-reinforced concrete beams. This paper aimed to investigate the effect of using ductile materials in the compression zone on the flexural performance of over-reinforced concrete beams. In order to avoid brittle compression failure, partial replacement of concrete with ductile materials layer in the compression zone was used. Four over-reinforced concrete beams of size $120 \times 180 \times 1,300$ mm were cast and tested under three-point loading conditions. The steel fibers reinforced concrete (SFRC),

slurry infiltrated fiber concrete (SIFCON), and ultra-high performance fiber reinforced concrete (UHPC) were used as ductile materials. The flexural capacity of the beams, failure modes, crack patterns, load-deflection relationships, ductility index, and toughness were investigated. The results showed that using ductile materials in the compression zone is an effective technique to increase the ultimate load, ductility, and toughness by up to 52.46, 84.78 and 279.93%, respectively, compared to the reference beam. In addition, the failure mode changed from brittle to ductile failure. Noting that the use of SFRC layer enhanced the ductility of over-reinforced concrete beams more than using UHPC and SIFCON layers. Also, one of the main advantages of this technique is led to increase the tensile reinforcement ratio up to 8.548% without needing the compressive reinforcement. Thus, ductile composite beams with a high flexural capacity were generated using an economical amount of ductile materials.

Hiba A. SAHIB✉

Ali K. AL-ASADI

Department of Civil Engineering, College of Engineering, University of Thi-Qar, Iraq

PREDICTION OF SHEAR STRENGTH OF CFRP-STRENGTHENED REINFORCED RECYCLED AGGREGATE CONCRETE BEAMS USING VARIOUS STRENGTHENING METHODS

Key words: strengthening, carbon fibre reinforced polymer, recycled concrete aggregates, reinforced concrete, stiffness, ductility

Introduction

The environmental problem of concrete can be traced to both existing buildings and structural waste whose useful lives have expired, meaning that they must be recycled or repurposed in significant quantities (Fahmy & Idriss, 2019). Thousands of concrete cubes, cylinders, and prisms are generated every day for laboratory testing or the construction of new buildings (Mussa, Abdulhadi, Abbood, Mutalib & Yaseen, 2020), all of which can also be considered waste material. Numerous researchers have consequently undertaken various studies to determine the practicality of employing re-

cycled aggregate concrete (RAC) manufactured from waste concrete in new construction projects. Utilizing RCA is crucial for conserving and safeguarding natural aggregate (NA). Numerous researchers have examined the impact of RCA concentrations on concrete compositions. In addition, a number of laboratories (Danraka, Mahmod, Oluwatosin & Student, 2017; Zhang et al., 2020; Mater, Elansary & Abdalla, 2022) have examined the behaviour of normal and high strength RAC relative to NA under various flexural and shear loading conditions. Obviously the durability of ordinary concrete differs from that of reprocessed concrete.

Many infrastructures, including buildings and bridges in war-torn nations like Iraq, have been devastated by the effects of war, terrorist attacks, explosives, progressive collapse, and other unforeseen events. The majority of the damaged structural components,

such as beams, columns, and slabs, have not collapsed completely and remain repairable. Today, carbon fibre reinforced polymer (CFRP) is commonly utilized to reinforce and retrofit structural members (Al-Saawani, El-Sayed & Al-Negheimish, 2020; Saadon, Mashrei & Al Qumari, 2022). Carbon fibre reinforced polymer can repair the load-bearing capability of damaged structural members, to make them usable once more.

This work involves an experimental investigation to study the effect of using CFRP to strengthen a beam cast with various replacement elements of RCA in a concrete mix, as a continuous part of an experimental investigation conducted by the author (Sahib & Al-Asadi, in press).

Research significance

The aim of the work is to study the shear strength of beams consisting of RAC, reinforced with CFRP when FRP strengthening is a possible option when the load carrying capacity of a structure must be increased due to design, damage or construction issues.

Materials and methods

Six reinforced concrete (RC) beams were cast, measuring 1,200 mm in length with a cross-section of 120 × 200 mm, with NA and RAC. The test was conducted using four-point loading. The geometry of the beams being tested is depicted in Figure 1. The reinforcing bars were made of 12 mm diameter steel, with three bars in tension, two in compression, and four stirrups being utilized to secure the longitudinal rebar (Fig. 2).

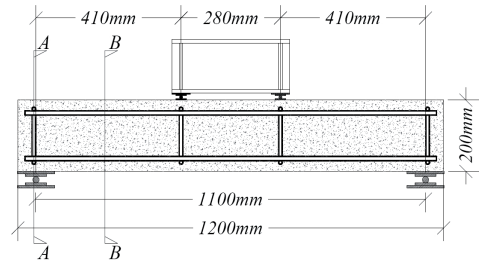


FIGURE 1. Geometry of the tested beams

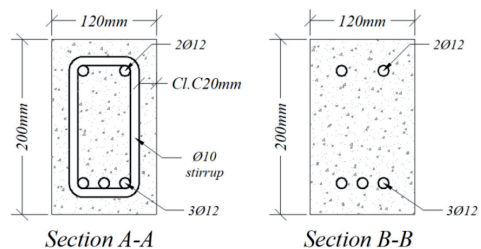


FIGURE 2. Reinforcement details of the tested beams

The experimented beams were divided into two groups according to the strengthening forms, inclination strips (IS) and continue strips (CS). Each group comprised three beams, with a replacement ratio of RCA 0%, 50% and 100%. Table 1 and Figures 3 and 4 show the data on the tested beams.

TABLE 1. Details of tested beams

Group	Replacement ratio [%]	Beam	Design
G1 IS form	0	B1	R0-IS
	50	B2	R50-IS
	100	B3	R100-IS
G2 CS form	0	B4	R0-CS
	50	B5	R50-CS
	100	B6	R100-CS

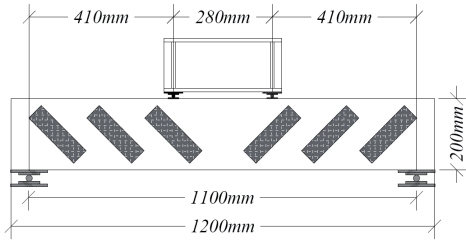


FIGURE 3. CFRP distribution for IS type beams

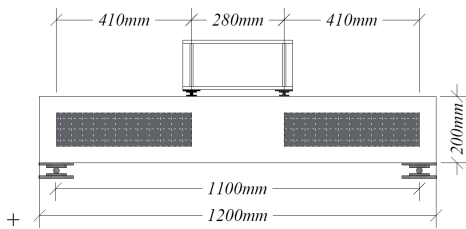


FIGURE 4. CFRP distribution for CS type beams

Materials

Cement

Ordinary Portland cement was used in this study. Both the physical and chemical results of the cement met the ASTM C150-15 requirements (ASTM International, 2015).

Sand

Prior to its use, the fine aggregate was tested according to the ASTM C136/C136M standard (ASTM International, 2006).

Natural and recycled concrete aggregate

It was decided to use crushed gravel with a maximum aggregate size of 19 mm as a natural aggregate (NA), while recycled concrete cubes that had been crushed were used as a recycled concrete aggregate (RCA), the grading satisfying the requirements of the ASTM C33/C33M-13 standard (ASTM International, 2013) for both materials (No 7).

Water

Potable water was used for all mixtures.

Steel reinforcement

The tensile test was used to determine the mechanical characteristics of the steel rebar. The results are summarized in Table 2. The results comply with the ASTM A615M-06b standard (ASTM International, 2004) (Grade 60).

Carbon fibre reinforced polymer (CFRP) and Sikadur®-330

A SikaWarp® Hex-300C unidirectional carbon fibre reinforced polymer strip was used to reinforce the concrete beam. Sikadur®-330 epoxy adhesive was used, comprising a primary base resin and hardener. Table 3 contains the manufacturer-supplied technical parameters of SikaWarp® Hex-300C strip and Sikadur®-330.

TABLE 2. Reinforcing steel test

Parameter	Steel sample		ASTM 615 limits
	Ø10 mm rebar	Ø12 mm rebar	
Yield stress [MPa]	573	560	≤ 420
Tensile strength [MPa]	672	635	≤ 620
Elongation [%]	16	15	≤ 9

TABLE 3. Properties of SikaWarp® Hex-300C sheets and Sikadur®-330

Material	Parameter	Result
Carbon fibre reinforced polymer	Tensile strength [MPa]	3 500
	Thickness [mm]	0.167
	Modulus of elasticity [GPa]	220
Epoxy	Elastic modulus [MPa]	4 500
	Tensile strength [MPa]	30
	Flexural modulus [MPa]	3 800

Tests

Mixing

Three different concrete mixes were utilized: natural aggregate concrete (M0-R0), 50% recycled concrete aggregate (M50-R50) and 100% recycled concrete aggregate (M100-R100). Each mixture was used to create reinforced beam specimens. The proportions of the concrete mix are shown in Table 4. Controlled use of the recycled and natural aggregate, as well as potable water, produced the desired compressive strength and workability (slump 6–8 cm).

Bonding of CFRP to concrete

The following steps were followed to bond the CFRP strip on each side of the concrete:

- increasing the surface roughness of the concrete with a steel brush;

- compressed air used to clean the concrete surface;
- use of a manual mixer to combine the two epoxy components;
- applying the epoxy paste to the surface of the CFRP strip;
- applying 2 mm of epoxy paste to the surface of the concrete;
- attaching the CFRP strip to the surface of the concrete;
- using a roller to release the air between the CFRP sheet and the epoxy.
- applying another layer of bonding material on top of the CFRP sheet, as shown in Figure 5.

Setup for the test

All specimens were tested using a hydraulically operated universal testing machine, “load controlled”, and were loaded to failure as shown in Figure 6. The deflections were

TABLE 4. Natural aggregate concrete and recycled aggregate concrete trial mix proportions

Mix content	Concrete		
	M0-R0	M50-R50	M100-R100
Cement [kg·m ⁻³]	430	430	430
Natural aggregate [kg·m ⁻³]	1 050	525	0
Recycled concrete aggregate [kg·m ⁻³]	0	525	1 050
Natural sand [kg·m ⁻³]	750	750	750
Water [kg·m ⁻³]	180	200	220
Slump [cm]	7.8	7.6	7.3



FIGURE 5. Sample with CFRP after bonding



FIGURE 6. Test equipment

measured during the tests using a linear variable displacement transducer (LVDT), while the load was measured using an electrical load cell.

Test results

Hardened concrete tests

Concrete compressive strength was determined after both 7 and 28 days of curing in water at 20°C, using 150 × 150 × 150 mm cubes. Three cubic specimens were used in each part of the experiment. The test results of the concrete compressive strength are shown in Table 5.

Table 5 demonstrates that the compressive strength of the concrete cubes decreases as the replacement ratio of RCA increases. Clearly, the compressive strength of RAC with 50% and 100% substitution fell by 9.5% and 13.4%, respectively, compared to the compressive strength of the natural aggregate concrete.

Fracture pattern and failure mechanisms

Figures 7–12 show the representative cracking pattern. The initial flexural crack on the beam began at the centre of the beam within the pure moment region at 22–28 kN or 25–32 kN, for strengthened beams with IS and CS forms respectively. In excess of this load, the cracks expanded toward the top fibre and more flexural cracks occurred along the length of the beam. At 35–50 kN, a shear angle fracture developed independently of the existing flexural cracks in the shear span zone. With a further load increase, the cracks

TABLE 5. Test results of concrete compressive strength (Sahib & Al-Asadi, in press)

Mix replacement ratio	Average compressive strength (28-day curing) [MPa]	Compressive strength [%]	Density [kg·m ⁻³]
R 0%	35.00	–	2 314.17
R 50%	31.67	–9.5	2 291.33
R 100%	30.31	–13.4	2 278.24

extended both towards the support and the load point, leading to a sudden, brittle shear failure and CFRP debonding, as shown in Figures 7–12 and Table 6.



FIGURE 7. Modes of failure of beam BM-R0-IS



FIGURE 8. Modes of failure of beam BM-R0-CS



FIGURE 9. Modes of failure of beam BM-R50-IS



FIGURE 10. Modes of failure of beam BM-R50-CS



FIGURE 11. Modes of failure of beam BM-R100-IS



FIGURE 12. Modes of failure of beam BM-R100-CS

Types of failure

According to Table 6, strengthening beams with CFRP in the form of VS (Sahib & Al-Asadi, in press), at the replacement ratios

TABLE 6. Summary of beam test results

Group	Specimen	Ultimate load [kN]	Increase/decrease in load capacity [%]	Ultimate deflection [mm]	Yield load [kN]	Mode of failure
G1a*	B1-R0%	65.12	–	5.57	52	shear failure
	B2-R50%	62.00	–	5.47	56	shear failure
	B3-R100%	53.85	–	5.80	47	shear failure
G2a*	B4-R0%-VS	71.34	9.50	6.14	50	CFRP debonding
	B5-R50%-VS	68.37	10.27	6.20	47	CFRP debonding
	B6-R100%-VS	61.66	14.50	6.18	50	CFRP debonding
G1b	B7-R0%-IS	76.27	17.10	6.25	60	CFRP debonding
	B8-R50%-IS	73.16	18.00	6.35	53	CFRP debonding
	B9-R100%-IS	64.18	19.18	6.48	50	CFRP debonding
G2b	B10-R0%-CS	88.55	35.90	5.69	71	CFRP debonding
	B11-R50%-CS	85.69	38.21	6.51	67	CFRP debonding
	B12-R100%-CS	75.39	40.00	6.00	60	CFRP debonding

*Results of G1a and G2a are taken from an article by Sahib and Al-Asadi (in press).

of RCA 0%, 50% and 100%, raised the ultimate load by 9.5–14.5%. Additionally, when strengthening beams with CFRP in the form of IS, the ultimate load increased by 14.5–40% at the replacement ratios of RCA 0%, 50% and 100%. The maximum load of beams strengthened in the CS form was 35.9–40% of the un-strengthened beam forms. These results show that strengthening using CFRP in the form of CS is particularly effective at improving the shear capacity of beams.

Load–displacement curve

Figures 13–16 depict the load–deflection curves of the 12 beam tests (6 beams from previous work and the other 6 from this work). All the beam specimens exhibited a comparable linear load–deflection response until the onset of the first flexural fracture, indicating the effect of gross section stiffness and the fact that the concrete contributed to the majority of the flexural resistance. Figure 13 compares the behaviour of beam specimens

with varied RCA ratios, and without strengthening. Figures 14–16 show the load deflection for three groups with strengthened beams (VS, IS and CS) and compare them with un-strengthened beams, where it is evident that the strengthened beams exhibited more ductile behaviour compared to the other beams. The CS form is very effective at improving the ultimate load of beams, as it uses the same amount of CFRP as the VS form and provides a high ultimate load and low deflection.

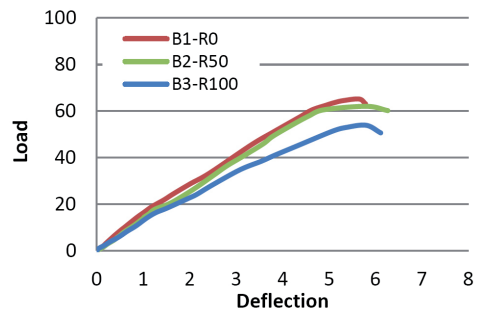


FIGURE 13. Load–deflection curve of un-strengthened beams (Sahib & Al-Asadi, in press)

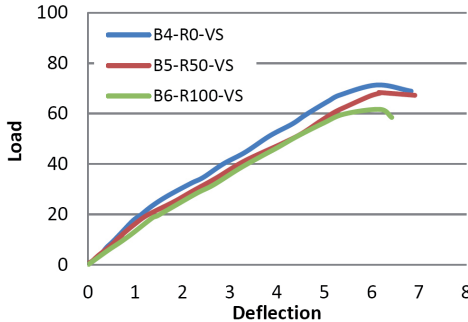


FIGURE 14. Load–deflection curve of beams strengthened with VS (Sahib & Al-Asadi, in press)

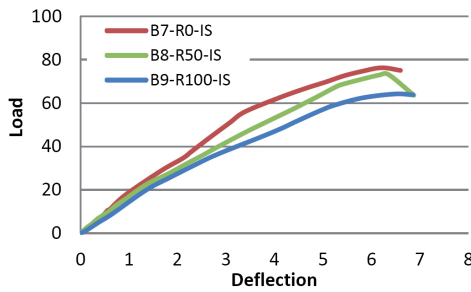


FIGURE 15. Load–deflection curve of beams strengthened with the IS form

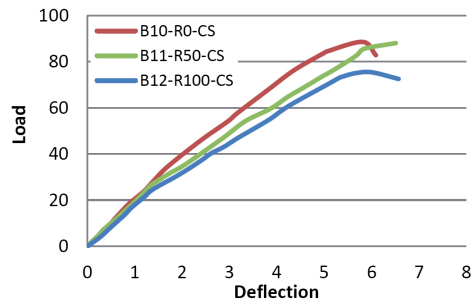


FIGURE 16. Load–deflection curve of beams strengthened with the CS form

First crack

Cracks were noticeable in the middle third after the applied force was shed, the first crack load being 18–32 kN for all beams. The visual first crack loads for the various beams are summarized in Table 7.

The beam results showed that the first crack loads increased by 16.67–39.13% when CFRP sheets were added to the beams, compared to the same beam without strengthening. The initial crack load increased as a result of strengthening the beams because CFRP had a role in confining the concrete and delaying the formation of cracks in the stress zone.

Stiffness test

The load versus deflection graphs in Figures 13–16, shows how different strengthening methods affect the flexural stiffness of the beams. The stiffness of the beams was defined as the slope of the line connecting the origin point and a point before the crack’s location in order to compare the results quantitatively. This means that the beam stiffness was defined as the slope of the load versus deflection curve when the beams were in the linear stage. The stiffness results for each beam are listed in Table 7. Compared to the control beams (B1, B2, B3), the stiffness of all the strengthened specimens increased. The average increases for groups two, three and four were 13.88%, 21.06% and 37.31% over the control beams, respectively. On the other hand, the stiffness of beams with a replacement ratio of 50% and 100% of the RCA decreased by 17.7% and 23.07% respectively. It can be concluded from the results that the stiffness value was affected by the percentage of recycled aggregate and the strengthening beam with CFRP, where it was decreased and increased by these effects respectively.

Ductility test

Ductility is defined as the ability of a member to withstand a load after failure (Anwar & Najam, 2016), and in the current study it was measured from the load deflec-

tion curve of the beam at mid span. This index was calculated using Eq. (1), as suggested in the literature (Pan, Kwan & Islam, 2001).

$$\mu = \frac{\Delta u}{\Delta y}, \quad (1)$$

where:

μ – ductility index of the beams,

Δu – ultimate deflection,

Δy – yield deflection.

The ductility index (μ) of the tested beams was calculated and is listed in Table 7. The yield deflection (Δy) is also presented in Table 7.

Beams strengthened with CFRP performed better in terms of ductility than un-strengthened beams, which can be attributed to the type of failure. It can be seen that the failure type of all the beams was a shear failure, which is defined as a brittle failure, thus by strengthening the shear capacity of the beam, the failure was pushed more to flexural failure, which could

be noticed from the strain values and crack pattern of the beam. The flexural failure is known to be a more ductile failure, hence the increase in the ductility value can be seen for the beam when the shear strength of the beam increases. The only exception was for beams with CFRP in the shape of CS, where the ductility decreased slightly from that of other strengthened beams, which might be due to the contribution of the CFRP in the flexural stiffness of the beam.

Conclusions

1. Strengthening the beams with CFRB increased the ultimate load carrying capacity.
2. Using CFRP increased the load capacity by an average of 11.42%, 18.09% and 38.04% for beams strengthened with VS, IS and CS forms respectively.
3. The use of the CS configuration was more effective than an IS scheme for beams strengthened with CFRP, where

TABLE 7. Ultimate deflection, yield deflection, stiffness, ductility and first crack load of tested beams

Group	Specimen	Ultimate deflection (Δu) [mm]	Yield deflection (Δy) [mm]	Stiffness (K_T) [%]	Ductility index (μ) [-]	First crack load (P_{cr}) [kN]
G1a	B1-R0%	5.57	3.85	16.90	1.45	23
	B2-R50%	5.47	4.47	13.91	1.22	20
	B3-R100%	5.80	4.12	13.00	1.41	18
G2a	B4-R0%-VS	6.14	3.79	18.74	1.62	29
	B5-R50%-VS	6.20	4.05	16.94	1.53	24
	B6-R100%-VS	6.18	4.37	14.17	1.41	26
G1b	B7-R0%-IS	6.25	3.87	19.65	1.61	28
	B8-R50%-IS	6.35	4.00	18.31	1.59	26
	B9-R100%-IS	6.48	4.29	14.99	1.51	22
G2b	B10-R0%-CS	5.69	3.81	21.79	1.49	32
	B11-R50%-CS	6.51	4.41	20.00	1.48	32
	B12-R100%-CS	6.00	4.18	18.10	1.44	25

the improvement in the ultimate load was 35.9–40% for a beam strengthened with the CS scheme, whereas the IS form increased the ultimate load by 17.1–19.18%, compared to un-strengthened beams.

4. The use of CFRP to strengthen beams was clear on the tangent stiffness value of the beams, where using VS forms increased the stiffness of the beam by 10.88%, 21.7% and 9% for an RCA replacement ratio of 0%, 50% and 100% respectively. In addition, the increase was 15.3–31.63% and 28.93–43.78% for IS and CS forms, respectively.
5. The ductility of beams strengthened with CFRP increased by an average of 8.48, 25.6 and 3.07 for beams strengthened with the VS, IS and CS forms respectively.

References

- Al-Saawani, M. A., El-Sayed, A. K., & Al-Negheimish, A. I. (2020). Effect of shear-span/depth ratio on debonding failures of FRP-strengthened RC beams. *Journal of Building Engineering*, 32, 101771. <https://doi.org/10.1016/j.jobe.2020.101771>.
- Anwar, N. & Najam, F. (2016). *Structural cross sections: analysis and design*. Oxford: Butterworth-Heinemann.
- ASTM International (2004). *Standard specification for deformed and plain carbon steel bars for concrete reinforcement* (ASTM A615/A615M-06b). West Conshohocken: ASTM International.
- ASTM International (2006). *Standard test method for sieve analysis of fine and coarse aggregates* (ASTM C136/C136M). West Conshohocken: American Society for Testing and Materials.
- ASTM International (2013). *Standard specification for concrete aggregates* (ASTM C33/C33M-13). West Conshohocken: ASTM International.
- ASTM International (2015). *Standard specification for portland cement* (ASTM C150/C150M-15). West Conshohocken: ASTM International.
- Danraka, M. N., Mahmud, H. M., Oluwatosin, O. K. J. & Student, P. (2017). Strengthening of reinforced concrete beams using FRP technique: a review. *International Journal of Engineering Science*, 7 (6), 13199.
- Fahmy, M. F. & Idriss, L. K. (2019). Flexural behavior of large scale semi-precast reinforced concrete T-beams made of natural and recycled aggregate concrete. *Engineering Structures*, 198, 109525. <https://doi.org/10.1016/j.engstruct.2019.109525>
- Mater, Y. M., Elansary, A. A. & Abdalla, H. A. (2022). Flexural behavior of recycled aggregate concrete beams strengthened with carbon fiber reinforced polymer. *Advances in Structural Engineering*, 25 (14), 13694332221113039. <https://doi.org/10.1177/13694332221113039>
- Mussa, M. H., Abdulhadi, A. M., Abbood, I. S., Mutalib, A. A. & Yaseen, Z. M. (2020). Late age dynamic strength of high-volume fly ash concrete with nano-silica and polypropylene fibres. *Crystals*, 10 (4), 243. <https://doi.org/10.3390/cryst10040243>
- Pam, H. J., Kwan, A. K. H. & Islam, M. S. (2001). Flexural strength and ductility of reinforced normal-and high-strength concrete beams. *Proceedings of the Institution of Civil Engineers-Structures and Buildings*, 146 (4), 381–389. <https://doi.org/10.1680/stbu.2002.152.4.361>
- Saadoon, A. M., Mashrei, M. A. & Al Oumari, K. A. (2022). Punching shear strength of recycled aggregate-steel fibrous concrete slabs with and without strengthening. *Advances in Structural Engineering*, 25 (10), 13694332221090288. <https://doi.org/10.1177/13694332221090288>
- Sahib, H. A. & Al-Asadi, A. K. (in press). *Shear behavior of recycled aggregate concrete beams strengthened by CFRP*.
- Zhang, G., Ali, Z. H., Aldemy, M. S., Mussa, M. H., Salih, S. Q., Hameed, M. M., Al-Khafaji, Z. & Yaseen, Z. M. (2020). Reinforced concrete deep beam shear strength capacity modelling using an integrative bio-inspired

algorithm with an artificial intelligence model. *Engineering with Computers*, 38, 1–14. <https://doi.org/10.1007/s00366-020-01137-1>

Summary

Prediction of shear strength of CFRP-strengthened reinforced recycled aggregate concrete beams using various strengthening methods. Fibre reinforced polymer (FRP) strengthening is a possible option when the load carrying capacity of a structure needs to be increased for various reasons. On the other hand, the focus nowadays aims to save the environment by reducing the waste material. A suggestion was made to use waste concrete as an aggregate. If this new material was used more, it would be possible to use recycled concrete aggregate

(RCA) and carbon fibre reinforced polymer (CFRP) to strengthen reinforced concrete (RC) structures and make them more environmentally friendly. An experimental investigation study on the shear behaviour of RC beams strengthened with CFRP strips was carried out. Tests were conducted on six reinforced concrete beams, with variations in the replacement ratio of RCA and strengthened by different configurations of CFRP under four-point loading. The results indicated that the load carrying capacity was increased, on average, by 18.09% and 35.04% for beams strengthened with CFRP with an inclined strip (IS) and continuous strip (CS) configurations respectively. The results also indicated that the increases in the stiffness were 21.08 and 37.31 for beams strengthened with CFRP in the IS and CS configurations, respectively. In addition the ductility of the beams increased after strengthening.

Ola Ahmed HUSSEIN¹  <https://orcid.org/0000-0003-2544-5033>

Aamer Najim ABBAS²  <https://orcid.org/0000-0001-5606-3439>

¹ Al-Rafidain University Collage, Department of Civil Engineering, Iraq

² University of Mustansiriyah, College of Engineering, Iraq

SELF-COMPACTING CONCRETE STRENGTHENING EFFICIENCY INVESTIGATION USING RECYCLED STEEL WASTE AS FIBRES

Key words: self-compacting concrete, waste steel fibre, compressive strength, recycling material, splitting tensile strength, adding recycled material

Introduction

There has been increased focus in recent years on recycling industrial manufacturing waste due to the massive amounts of pollution that is predicted as a result of industrial operations and its detrimental impact on the environment.

In general, there have been many studies on reusing waste material in concrete, such as carpet waste, used tires, polypropylene and nylon, wood fibre as paper product waste, steel shavings as an alternative to steel fibres (Wang, Wu & Li, 2000), and iron

waste (Ghannam, Najm & Vasconez, 2016) to benefit from waste material while improving the properties and performance and lowering costs by including the recycled fibre into the process as a substitute for manufactured fibres to avoid disposing of waste in landfills.

Steel fibres are commonly utilized in structural facilities as well as other applications. Slope stabilization is a term used to describe the process of making a slope more stable. Artificial fibres improve the efficiency of the concrete, but they are not without their drawbacks. Produced from non-renewable and expensive materials, the steel industry generates large quantities of steel waste materials, which can be environmentally damaging if left untreated (Merli, Preziosi, Acampara, Lucchetti & Petrucci, 2020).

The primary waste products from steel product manufacturing, which offer severe concerns across the world, may be reduced by using it as a resource, such as by turning machine recyclable materials into fibre for concrete. The use of certain wastes in concrete is considered a safe resource (Prasad, Maanvit, Jagarapu & Eluru, 2020).

Mohammadi, Singh and Kaushik (2008) discussed steel waste fibre as an admixture material in concrete, which was an appealing choice as steel waste has high strength and durability, which could lead to an increase in the strength of the concrete as well as improving some of its properties, such as ductility, impact resistance and dynamic load resistance, as well as delaying the evolution of macro cracks, especially their width.

Aghaee and Yazdi (2014) used waste steel wire from rebar and wooden moulds previously used in construction projects in lightweight structural concrete (SLWC) testing. To assess the mechanical characteristics of 28-day reinforced lightweight concrete samples using waste wire, a series of tensile, flexural, and impact tests were conducted. In the volume fraction of concrete, the percentage of wire in fibre-reinforced concrete was 0.25%, 0.5% and 0.75%. The findings show that concrete's bending, tensile, and impact characteristics may be significantly enhanced through the use of discarded wire. The use of scrap steel wire as a suitable fine reinforcement in lightweight concrete is also concluded.

In general, it is understood that fibre-reinforced concrete, which uses a variety of metallic, hybrid, and polymeric fibres, may enhance the behaviour of concrete

when it has cracked by bridging the fractures, reducing the energy consumption and enhancing the ductility capacity of the concrete elements.

Jang and Yun (2018) investigated the effect of steel fibre content and coarse aggregate size on the mechanical properties of high strength concrete. The research also showed the relationship between compressive strength and bending strength of high strength steel fibre reinforced concrete (SFRC) used in four ratios: 0.5%, 1%, 1.5% and 2%. Compression and bending tests were performed, and the results were then used to verify the effect of the steel fibre volume fraction and the total volume on the SFRC's compressive, flexural and bending hardness, which increased significantly with increasing steel fibre ratio. Also, the equations that have been proposed to determine the compressive stiffness ratio based on the equivalent flexural strength ratio were used to predict the mechanical properties of SFRC in this study.

Orouji, Zahrai and Najaf (2021) added different quantities of glass fibre and polypropylene fibre to investigate their effect on the compression and flexural strength of lightweight concrete. The percentages of glass were 20%, 25% and 30%, while the percentages of used polypropylene fibres were 0.5%, 0.75%, 1%, 1.5% and 2%. The increase in the compressive strength, flexural strength, and ductility of the tested specimens were reached about 1.6, 4.0 and 13.2 times, respectively.

Najaf, Abbasi and Zahrai (2022) studied the effect of using waste glass powder, polypropylene fibres and microsilica to manufacture lightweight and sustainable

concrete with high compressive and bending strength, ductility, and impact resistance.

The objective of this research was to investigate the efficiency of recycled steel scrap as a fibre on the mechanical characteristics of self-compacting concrete. The more highlighted goal was to evaluate the optimal amount and percentage of steel scrap and also to investigate the variation in the mechanical properties of concrete with time. As a result, more research is needed on the strength of concrete as well as how to estimate the best rates for adding recycled steel waste.

The goal of the study was to examine how effectively self-compacting concrete's mechanical properties can perform when recycled steel is used as a fibrous reinforcing material.

Experimental program

The implications were studied of adding steel waste on the mechanical characteristics of self-compacting concrete. Waste steel scrap was used as fibres to strengthen concrete. Compressive and splitting tensile strengths were the properties studied, as well as their effect on strength development over time. Slump test concrete workability diminishes according to the fraction of recycled steel scrap that is added (Sharma & Ahuja, 2015).

Materials specifications

Cement

Tables 1 and 2 illustrate the cement properties that were used to manufacture the concrete. Ordinary Portland cement was adopted.

The physical characteristics of the cement were tested using the standards established by ASTM International (formerly known as American Society for Testing and Materials): ASTM C184-94e1 (2020b), ASTM C187-16 (2020c), ASTM C188-17 (2020d) and ASTM C19-19 (2020a).

TABLE 1. Chemical analysis of the cement

Chemical element	Test result [%]	Specification limit [%]
SiO ₂	22.40	–
Al ₂ O ₃	5.78	–
Fe ₂ O ₃	3.24	–
CaO	66.55	–
MgO	3.98	≥ 5.0
SO ₃	2.23	≥ 2.5
LOI	3.11	≥ 4.0
IR	0.98	0.66–1.02
C ₃ A	2.89	≥ 3.5

TABLE 2. Physical test results of cement

Test item	Test result	Specification limit
Initial setting [min]	112	≤ 45
Final setting [min]	334	≤ 600
Soundness expansion, le Chatelier [mm]	1.4	≤ 10
Compressive strength (3 day curing) [MPa]	15.39	≤ 15.00
Compressive strength (7 day curing) [MPa]	24.10	≤ 23.00

Sand

A fine aggregate, which was natural sand, had a fineness modulus of 2.65. The particles of sand larger than 4.75 mm were eliminated via sieve analysis (Table 3).

TABLE 3. Test results of sand

Opening size [mm]	Passing [%]	Specification			
		A	B	C	D
9.5	100.00	100	100	100	100
4.75	98.99	90–100	90–100	85–100	95–100
2.36	89.22	60–95	75–100	85–100	95–100
1.18	75.68	30–70	55–90	75–100	90–100
0.6	53.88	34–15	35–59	60–79	80–100
0.3	17.79	20–5	8–30	12–40	15–50
0.15	3.01	0–10	0–10	0–10	0–10
SO ₃	Test result	Specification			
	0.41%	< 0.50%			

Gravel

Crushed coarse aggregate was used, with a maximum size of 19 mm and a fineness modulus of 2.7. The gradation of the coarse aggregate's proportionate particle sizes was assessed by sieve analysis (Table 4).

Plasticizer

To avoid a negative effect, a superplasticizer was added to the concrete mix. The superplasticizer, SEKA 5390, conforms to the ASTM C494 standard (ASTM, 2012).

Steel waste

Steel fibres have a detrimental impact on workability; but despite this they improve

the mechanical characteristics of concrete (Ulas, Alyamac & Ulucan, 2017).

As illustrated in Figure 1, discarded steel waste was selected for mixing purposes. Since waste steel scrap performs well as steel fibre in concrete, the aspect ratio (length to diameter) was set at 50–60 according to the ACI 544.3R-93 standard related to steel fibres (American Concrete Institution [ACI], 1993). The material qualities of the primary structural steel are passed down to the waste steel, and to meet this requirement the steel wastes were cut to a size that did not exceed 0.9525 cm (see Figure 1).

Poisson's ratio was 0.3, the modulus of elasticity was 200 MPa, and the relative density was 7,850 kg·m⁻³.

TABLE 4. Test results of gravel

Opening size [mm]	Passing [%]	Specification		
		5–40 [mm]	5–20 [mm]	5–14 [mm]
37.5	100.00	95–100	100	–
19.0	98.10	35–70	95–100	100
9.5	42.30	10–40	30–60	50–80
4.75	8.60	0–5	0–10	0–10
SO ₃	Test result	Specification		
	0.41%	< 0.10%		



FIGURE 1. Technique for processing recycled steel fibre



FIGURE 2. Preparing samples groups for testing

Mix design

The mix design was carried out in accordance with the ACI 544.3R-93 standard (ACI, 1993). All material quantities are described in Table 5.

Specimen preparation

The work addressed three groups of concrete, labelled: Ws0, Ws1 and Ws1.5, which were without steel waste fibre addition (Ws0), with 1% steel waste fibre addition (Ws1), and with 1.5% steel waste fibre addition (Ws1.5).

Concrete samples were stored for 28 days in a water pool for curing. Figure 2 shows samples during preparation.

Experimental tests

Compressive strength test

To investigate the compressive strength of the concrete, standard cube specimens were used, with dimensions of $15 \times 15 \times 15$ cm in accordance with the ACI 544.2R-89 standard (ACI, 1989). A uniaxial compression test was constructed. The compressive strength

TABLE 5. Quantity of materials for the designated concrete sample groups

Group	Cement [kg·m ⁻³]	Sand [kg·m ⁻³]	Crushed gravel [kg·m ⁻³]	w/c	Superplasticizer SEKA 5390 [%]	Steel waste fibre [%]
Ws0	380	750	1 024	0.38	0.8	0
Ws1	380	750	1 024	0.38	0.8	1.0
Ws1.5	380	750	1 024	0.38	0.8	1.5

of concrete grade C-30 was the intended result. Concrete with volumetric ratio of steel waste fibres was the variable. Three steel waste volumetric ratios were evaluated: 0%, 1% and 1.5%.

The compressive strength of the cube sample was calculated by the following equation:

$$f_{\text{comp.}} = \frac{P_C}{A}, \quad (1)$$

P_C – compression failure load [kN],
 A – loaded area of cube [cm²].

The compressive tests, as shown in Figure 3, were conducted after 7, 14 and 28 days of dipping in water for curing.

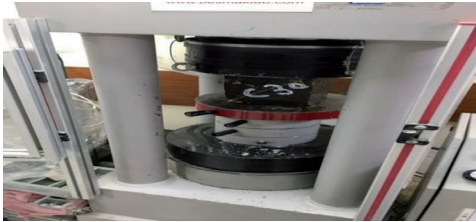


FIGURE 3. Compressive strength test

Tensile strength test

For tensile strength, sample cylinders with a diameter of 15 cm and a length of 30 cm all underwent splitting tests, with a target load of 1.2 mPa·s⁻¹. The set up for the splitting test is shown in Figure 4. The test was run in accordance with the ASTM C496-86 standard (ASTM, 1986).

The compressive load of the cylinder sample was calculated by the following equation:

$$f_{\text{split.}} = \frac{2P}{\pi DL}, \quad (2)$$

P – compressive load [kN],

D – diameter of cylinder sample [cm],

L – length of cylinder sample [cm].

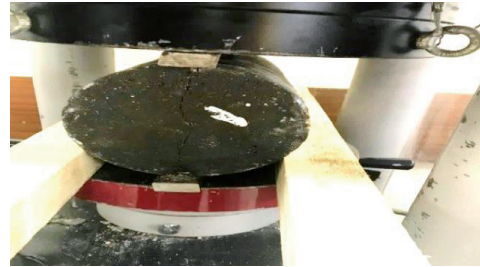


FIGURE 4. Splitting tensile test

Results

Compression strength

The compressive strengths from the samples tests are listed in Table 6, for the day 7, day 14 and day 28 samples for groups Ws0, Ws1 and Ws1.5. The average compressive strengths given in Figure 5 is for the day 14 samples. Figure 6 represented the average compressive strength at day 28.

The uniaxial compression test shows that the 1% steel waste increases in compressive strength on day 28 by 12% as a result of the bridging effect of the steel waste, where the cracks had difficulty in extending. The 1.5% steel waste only increased the compressive strength by 0.35% in comparison with the specimen without steel waste on day 28.

TABLE 6. Average compressive strength on days 7, 14 and 28, for the Ws0, Ws1, Ws1.5 sample groups

Group	Density [kg·m ⁻³]	Water content [%]	Average compressive strength on day 7 [MPa]	Average compressive strength on day 14 [MPa]	Average compressive strength on day 28 [MPa]
Ws0	2 350	144.4	30.68	36.56	43.83
Ws1	2 691	144.4	35.00	38.66	49.15
Ws1.5	2 788	144.4	30.80	40.00	44.00

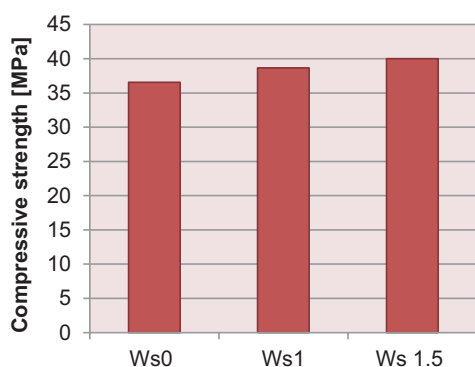


FIGURE 5. Average compressive strengths for samples groups Ws0, Ws1, Ws1.5 on curing day 14

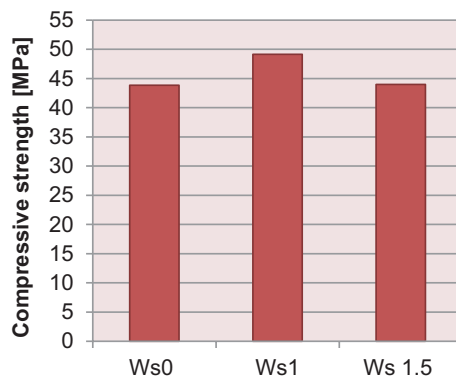


FIGURE 6. Average compressive strengths for samples groups Ws0, Ws1, Ws1.5 on curing day 28

The reason for the low difference in the compressive strength is that the low strength of concrete, corresponding to the high strength of steel fibres, causes severe spalling of the concrete around the splitting hole of the fibres. The results from the experiment are compiled in Table 6.

Tensile strength

The results of the tensile strength are given in Table 7 for days 7, 14 and 28 for groups Ws0, Ws1 and Ws1.5. The average tensile strength values are given in Figure 7 for day 14, the average Ws was 2.92, as well

TABLE 7. Average tensile strength on days 7, 14 and 28, for the Ws0, Ws1, Ws1.5 sample groups

Group	Average tensile strength on day 7 [MPa]	Average tensile strength on day 14 [MPa]	Average tensile strength on day 28 [MPa]
Ws0	2.23	2.92	3.18
Ws1	2.78	3.498	3.91
Ws1.5	2.87	3.63	4.10



FIGURE 7. Average tensile strengths for sample groups Ws0, Ws1, Ws1.5 on day 14 of curing

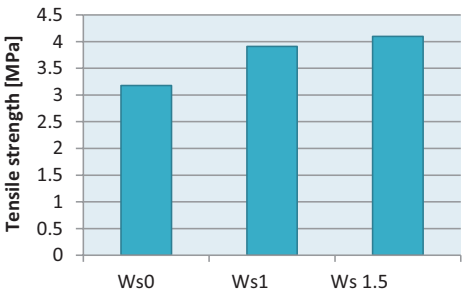


FIGURE 8. Average tensile strengths for sample groups Ws0, Ws1, Ws1.5 on day 28 of curing

as 3.5 and 3.63 for Ws1 and Ws1.5 respectively. The reason for this was the increased interlocking between the components of the concrete mixture by increasing the percentage of fibres in the concrete mixture, which in turn delayed the appearance of cracks and reduced their width. Fibres also have a major role in forming connecting bridges in the crack area to help increase endurance and create additional tensile resistance. While Figure 8 gives the average tensile strength at the day 28 point, which was 3.18, 3.91, and 4.1 for Ws0, Ws1 and Ws1.5, respectively.

Development of strength with age

Figure 9 illustrates the relationships between compressive strength development of the strength on days 0, 7, 14 and

28, and it was indicated that on day 14 the average strength of group Ws1 and Ws1.5 was more than group Ws0, without waste steel fibre, would achieve on day 28, with Ws1 achieving the highest value and Ws1.5 close to Ws0.

Figure 10 shows the relationship between tensile strength development and the strength on days 0, 7, 14 and 28, and it is indicated that on day 14 the average strength of group Ws1.5 achieved a value equal to the highest by Ws1, and this was also more than group Ws0, and it was also shown that Ws1.5 on day 28 achieved the highest value.

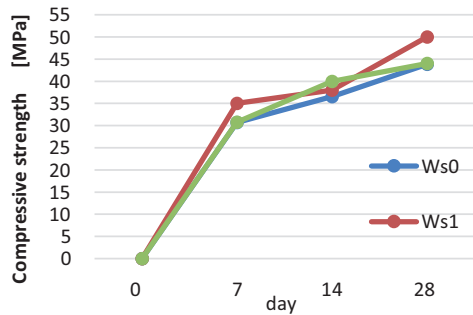


FIGURE 9. Development of compressive strength on days 0, 7, 14 and 28 for Ws0, Ws1 and Ws1.5

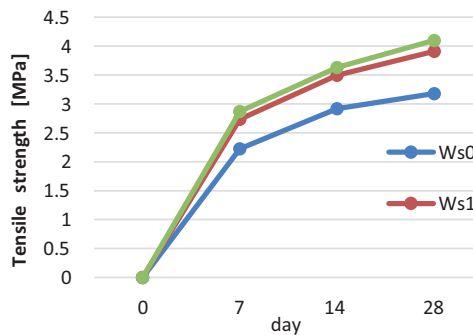


FIGURE 10. Development of tensile strength on days 0, 7, 14 and 28 for Ws0, Ws1 and Ws1.5

Conclusions

The results obtained for concrete samples containing fibres in different volumetric ratios led to the following points:

1. Addition of waste steel fibres has an effect on the compressive strength of concrete, but its effect was more pronounced on the tensile strength.
2. By increasing the percentage of fibres, the tensile strength improved up to 29% when 1.5% of steel fibres was added to concrete.
3. The addition of fibres to concrete contributed to reducing the occurrence of cracks and their widening, by creating bridges that connected the elements of the concrete. The addition of fibres also led to a change in the collapse pattern, from a brittle to a ductile failure.
4. The rate of achieving the compressive strength over time in the case of 1% of waste fibres is higher when compared with the specimens without fibres or the specimens containing 1.5% of waste fibres.
5. It was detected that the development in tensile strength was more when using 1.5% of fibres, compared to the specimens without fibres and the specimens containing 1% of fibres.

References

- Aghaee, K. & Yazdi, M. A. (2014). Waste steel wires modified structural lightweight concrete. *Materials Research*, 17 (4), 958–966. <https://doi.org/10.1590/1516-1439.257413>
- American Concrete Institution [ACI] (1984). *Measurement of properties of fiber reinforced concrete* (ACI 544.2R-89). Farmington Hills: American Concrete Institution.
- American Concrete Institution [ACI] (1993). *Guide for specifying, proportioning, mixing, placing, and finishing steel fiber reinforced concrete* (ACI 544.3R-93). Farmington Hills: American Concrete Institution.
- American Society for Testing and Materials [ASTM] (1986). ASTM C496-86. Standard test method for splitting tensile strength of cylindrical concrete specimens. In *Annual Book of ASTM Standards*. Philadelphia: American Society for Testing and Materials.
- ASTM International [ASTM] (2012). *Standard specification for chemical admixtures for concrete; chemical admixture; compressive strength; performance requirements; statistical analysis* (ASTM C494). West Conshohocken: ASTM International.
- ASTM International [ASTM] (2020a). *Standard test methods for time of setting of hydraulic cement by Vicat needle* (ASTM C191-19). West Conshohocken: ASTM International. Retrieved from: <https://www.astm.org/Standards/C191>
- ASTM International [ASTM] (2020b). *Standard test method for fineness of hydraulic cement by the 150-mm (No. 100) and 75-mm (No. 200) sieves (withdrawn 2002)* (ASTM C184-94e1). West Conshohocken: ASTM International. Retrieved from: <https://www.astm.org/Standards/C184>
- ASTM International [ASTM] (2020c). *Standard test method for amount of water required for normal consistency of hydraulic cement paste* (ASTM C187-16). West Conshohocken: ASTM International. Retrieved from: <https://www.astm.org/Standards/C187>
- ASTM International [ASTM] (2020d). *Standard test method for density of hydraulic cement* (ASTM C188-17). West Conshohocken: ASTM International. Retrieved from: <https://www.astm.org/Standards/C188>
- Ghannam, S., Najm, H. & Vasconez, R. (2016). Experimental study of concrete made with granite and iron powders as partial replacement of sand. *Sustainable Materials and Technologies*, 9, 1–9. <https://doi.org/10.1016/j.susmat.2016.06.001>
- Jang, S. J. & Yun, H. D. (2018). Combined effects of steel fiber and coarse aggregate size on the compressive and flexural toughness of

- high-strength concrete. *Composite Structures*, 185, 203–211. <https://doi.org/10.1016/j.compstruct.2017.11.009>
- Merli, R., Preziosi, M., Acampora, A., Lucchetti, M. C. & Petrucci, E. (2020). Recycled fibers in reinforced concrete: a systematic literature review. *Journal of Cleaner Production*, 248, 119207. <https://doi.org/10.1016/j.jclepro.2019.119207>
- Mohammadi, Y., Singh, S. P. & Kaushik, S. K. (2008). Properties of steel fibrous concrete containing mixed fibers in fresh and hardened states. *Journal of Construction and Building Materials*, 22 (5), 956–965. <https://doi.org/10.1016/j.conbuildmat.2006.12.004>
- Najaf, E., Abbasi, H. & Zahrai, S. M. (2022). Effect of waste glass powder, microsilica and polypropylene fibers on ductility, flexural and impact strengths of lightweight concrete. *International Journal of Structural Integrity*, 13 (1), 511–533. <https://doi.org/10.1108/IJSI-03-2022-0039>
- Orouji, M., Zahrai, S. M. & Najaf, E. (2021). Effect of glass powder & polypropylene fibers on compressive and flexural strengths, toughness and ductility of concrete: an environmental approach. *Structures*, 33, 4616–4628. <https://doi.org/10.1016/j.istruc.2021.07.048>
- Prasad, B. P., Maanvit, P. S., Jagarapu, D. C. K. & Eluru, A. (2020). Flexural behavior of fiber reinforced concrete incorporation with lathe steel scrap. *Materials Today: Proceedings*, 33, 196–200. <https://doi.org/10.1016/j.matpr.2020.03.793>
- Sharma, U. & Ahuja, R. (2015). Evaluation of workability and cracking pattern in flexure of steel fibre reinforced concrete (SFRC). *Journal of Civil Engineering and Environmental Technology*, 2 (9), 2349–8404.
- Ulas, M. A., Alyamac, K. E. & Ulucan, Z. C. (2017). Effects of aggregate grading on the properties of steel fibre-reinforced concrete. *IOP Conference Series: Materials Science and Engineering*, 246 (1), 012015. <http://dx.doi.org/10.1088/1757-899X/246/1/012015>
- Wang, Y., Wu, H. C. & Li, V. C. (2000). Concrete Reinforcement with Recycled Fibers. *Journal of Materials in Civil Engineering*, 12 (4), 314–319. [https://doi.org/10.1061/\(asce\)0899-1561\(2000\)12:4\(314\)](https://doi.org/10.1061/(asce)0899-1561(2000)12:4(314))

Summary

Self-compacting concrete strengthening efficiency investigation using recycled steel waste as fibres. Steel recycling saves energy and time, and is more environmentally friendly. It can help rid the environment of huge amounts of scrap vehicles and huge structures, as well as reducing the mining operations that destroy the natural environment. In this investigation, the steel scrap effect on the mechanical properties of concrete was investigated, in addition to investigating the variation in mechanical properties with increased concrete age. Three concrete mixes were studied: one without steel waste as a control, one with 1% steel waste by volume of concrete, and one with 1.5% steel waste by volume of concrete. The results show that adding waste steel to the concrete improved the compressive strength as well as the tensile strength, where a mixture which contains 1% of steel waste had an increase in strength of up to 12% and 23% by day 28 for compressive strength, and tensile strength sequentially in comparison to the reference mix. Furthermore, the results show that there was a significant increase in splitting tensile strength, at 29% on day 28 for a mix of 1.5% steel waste as compared to the reference concrete mix. The best improvement in compressive strength over time was obtained when using 1% steel waste. The best improvement in tensile strength over time was obtained when using 1.5% of steel waste. In both cases, the amount of the improvement was better than the models without steel waste, which gives us confidence in giving recommendations for conducting more in-depth studies to achieve the maximum advantage.

Malak H. DAWOOD✉

Ali K. Al-ASADI

Department of Civil Engineering, College of Engineering, University of Thi-Qar, Iraq

MECHANICAL PROPERTIES AND FLEXURAL BEHAVIOUR OF REINFORCED CONCRETE BEAMS CONTAINING RECYCLED CONCRETE AGGREGATE

Key words: normal aggregate (NA), recycled concrete aggregate (RCA), reinforced concrete (RC), interfacial transition zone (ITZ)

Introduction

Construction and demolition (C&D) waste is one of the most solid types of waste to accumulate annually in large quantities, because it has high durability, does not break down or decompose naturally, and thus becomes an internationally growing pollution problem with every passing year. Sweden, for example, annually produces about 1.5 M t of construction waste (Karlsson, 1998) while Poland produces 3.5 M t. One of the methods currently used to recycle this waste is to use it to replace natural aggregates, to produce new concrete by breaking clean blocks that do not contain

wood, rebar, or gypsum product residues, into sizes similar to gravel granules, and then washing and staging them, i.e. separating them using sieves into different sizes. It is called recycled concrete aggregate (RCA) and has the properties of the concrete from which it was produced and contains the same components (Bołtryk, Małasz-kiewicz & Pawluczyk, 2007). Choosing a well-recycled aggregate source can improve the properties of fresh concrete. Unlike natural aggregate (NA), recycled aggregate contains a large number of micro-cracks as a result of the crushing process. In addition, it may have old mortar attached to its surface. This means that an interfacial transition zone (ITZ) may form between the old mortar and the original aggregate, as shown in Figure 1, which is a weak region in RCA. That is why the quality of recycled aggregate is low.

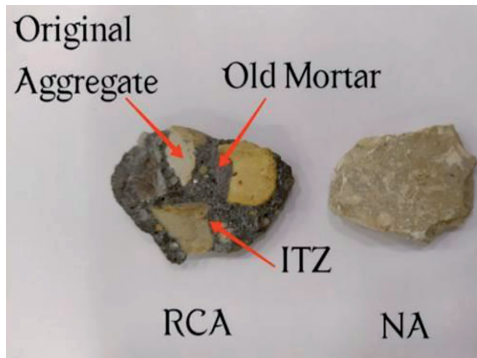


FIGURE 1. The difference between the natural and recycled aggregate

This paper explores the effect of RCA replacement ratio on the mechanical properties and flexural behaviour of reinforced concrete (RC) beams using RCA. Throughout the work, various RCA replacement levels and reinforcement ratios were used. Xiao, Li, Fan and Huang (2012) reported that changes in compressive strength are mostly a function of RCA quality, which may result in a variety of compressive strength results, including no change, a decrease in strength, or even an increase in strength in comparison to reference specimens. However, it is mostly reported that a reduction in water-to-cement ratio and an increase in cementation material content increases RCA's compressive strength. Meddah, Al-Harthy and Ismail (2020) indicated that the adoption of RCA as a partial or total replacement for NA has decreased the flexural strength of concrete. The reduction in flexural strength of RCA-concrete relates to the weakened bonding strength between the aggregate fraction and cement paste. The weakness of ITZ is significantly related to the characteristics of RCA. The bonding strength between the aggregate

and cement paste is significantly weakened due to the porosity and poor strength of the old mortar found in the RCA. Yang, Park, Kim and Lee (2020) investigated the flexural behaviour of concrete beams based on RCA. The RCA contents were 30%, 50% and 100%, and tensile rebar ratios were 0.50%, 0.79% and 1.14%. The results of the tests showed that the number of cracks was greater in the RCA beams than in the NA beams. Consequently, the cracking pattern showed that the RCA beams had, in general, closer crack spacing than the NC beams. Flexural strength values of RCA beams with low reinforcement bar ratios of 0.50% and 0.79% decreased significantly as the RCA content increased. On the other hand, the influence of RCA content on the flexural strength of beams with a high reinforcement bar ratio of 1.14% was not noticeable. Moreover, the RCA content had no noticeable effect on the ductility index. The ductility of the RCA beams increased as the RCA content increased.

The purpose of this study is to assess the mechanical properties of plain concrete by partial replacement with RCA 30%, 50% and 70% by weight, and the flexural performance of RCA beams. The effect of the RCA ratio on compressive, splitting, and flexural strengths are also discussed. Both the crack patterns and load carrying capacity for RC beams are given.

Experimental program

The experimental work included evaluating the mechanical properties and flexural capacity as well as the behaviour of beams with natural and recycled aggregates.

Materials and concrete mix design

Cement (CEM I 42.5N), sand, NA and RCA were collected from crushed old concrete cubes, with steel being used for casting and reinforcing beam specimens throughout the current study. Table 1 shows the designed proportion ratios. The electrical mixer used throughout the work is shown in Figure 2a. The slump test was performed to measure the workability of fresh concrete, as shown in Figure 2b, conducted on fresh concrete immediately after it was taken from the mixer.

aggregate conformed with the specifications of ASTM C33 (ASTM International, 2003). The steel reinforcement has been tested according to the ASTM A615/A615M standard (ASTM International, 2022). Table 2 shows the properties of the materials used.

Details of the beams

The experimental program consisted of four RC beams, one of them being the control beam made from normal concrete (NC) while the other beams contained 30%, 50%

TABLE 1. Mix design proportion ratios

Concrete mix	Cement [kg·m ⁻³]	w/c	Water [kg·m ⁻³]	Fine aggregate [kg·m ⁻³]	Coarse aggregate [kg·m ⁻³]	
					NA	RCA
NC	465	0.44	204.60	645	1 095.0	–
RCA 30%	465	0.47	218.55	645	766.5	328.5
RCA 50%	465	0.49	227.85	645	547.5	547.5
RCA 70%	465	0.51	237.15	645	328.5	766.5

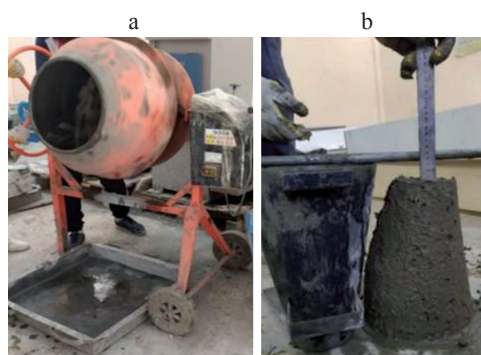


FIGURE 2. Preparing fresh concrete: concrete mixer (a); lump test (b)

The cement used conformed to the specifications of ASTM C150/C150M (ASTM International, 2015). The coarse and fine

TABLE 2. Properties of the materials

Material	Property	Value	
Cement	Average compressive strength, aged 7 days [MPa]	23.8	
Steel	Ø12	Yield strength [MPa]	565
		Ultimate strength [MPa]	687
	Ø10	Yield strength [MPa]	622
		Ultimate strength [MPa]	746
Sand	Sulphate (SO ₃) [%]	0.498	
Natural aggregate	Bulk density [g·cm ⁻³]	1.569	
	Water absorption [%]	1	
	Max size [mm]	19	
Recycled aggregate	Bulk density [g·cm ⁻³]	1.466	
	Water absorption [%]	5	
	Maximum size [mm]	19	

and 70% RCA. The reinforcement details of the tested beams are shown in Figure 3. All beams were simply supported and tested under a four-point load.

Casting and curing

Three layers of concrete were cast in the mould. Each layer was compacted using an electrical vibrating table to ensure

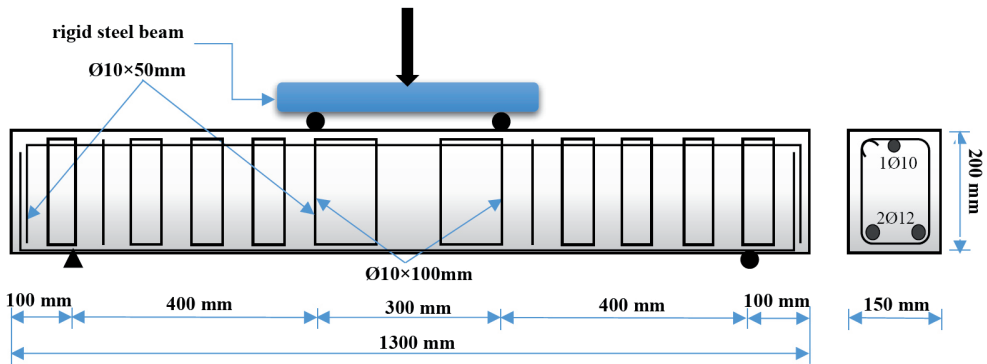


FIGURE 3. Specimen dimensions and details of steel reinforcement

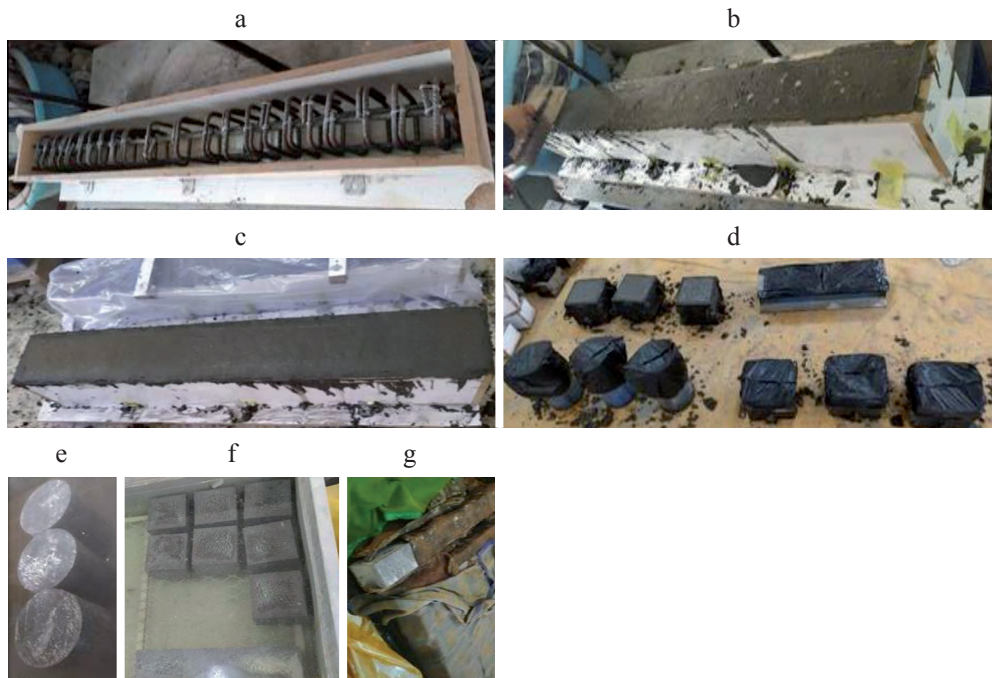


FIGURE 4. The process of casting and curing: fixing steel reinforcement in the mould (a); compacting the specimen and finishing the surface (b); covering the specimen with polyethylene sheets (c); covering the samples with polyethylene sheets (d); curing the samples in water (f–e); covering and curing of beams under wet canvas (g)

that no air was trapped inside. The top surface was smoothed by a steel trowel. Additionally, each batch included three cubes ($150 \times 150 \times 150$ mm), three standard cylinders (300×150 mm), and one prism ($100 \times 100 \times 500$ mm). All specimens (beams, cubes, cylinders and prisms) were covered with polyethylene sheets after casting to prevent water evaporation. After 36 h, the moulds were removed and the beams were cured in the laboratory by covering them with wet canvas until the testing age of 28 days. Figure 4 shows the process of casting and curing.

Results and discussions

This section presents and discusses the results of the cubes, cylinders and prisms, as well as flexural testing on four RC beams. The results include compressive strength, stress–strain curve, flexural strength, splitting tensile strength, crack pattern, failure mode, load capacity and mid-span deflection for each of the tested beams.

Properties of fresh concrete (workability)

The slump results for different mixes are shown in Figure 5. It can be seen that as the replacement ratio of RCA increased,

the slump value of RCA fresh concrete decreased by 26.3%, 42.1% and 57.9% for RCA 30%, 50% and 70% respectively, compared to the normal concrete, due to the relatively large water absorption and rough surface of the RCA.

Mechanical properties of hardened concrete

In general, it is noticeable that the mechanical properties of RCA concrete decrease in varying proportions compared to normal concrete, and this is in agreement with the results reported by Saadon, Mashrei and Al Qumari (2022). This is because the ITZ between RCA and cement paste was weaker than that between NA and the paste. All tests were performed after 28 days of curing.

Compressive strength

Table 3 illustrates that the compressive strength of concrete cubes typically decreases with increasing the replacement ratio of RCA. The compressive strength of RCA concrete with the replacement of 30%, 50% and 70% decreased by 9.10%, 18.88% and 22.57% respectively, compared to the compressive strength of normal concrete.

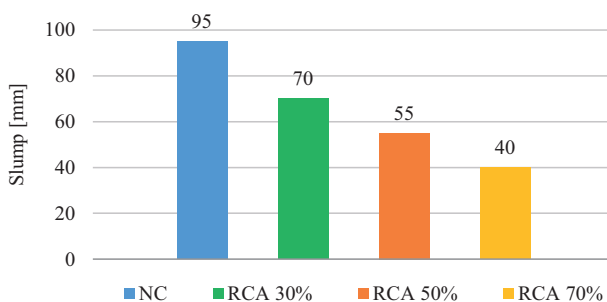


FIGURE 5. Slump results

TABLE 3. Compressive strength results for cubes

Concrete mix	Average cubic compressive strength (f_{cu}) [MPa]	Decrease in compressive strength [%]
NC	42.30	–
RCA 30%	38.45	9.10
RCA 50%	34.31	18.88
RCA 70%	32.75	22.57

Stress–strain curve

Figure 6 shows the stress–strain relations of NC and RCA mixes with RCA ratios (30%, 50% and 70%). It can be seen that the behaviour of all the specimens differed slightly throughout the first stage (linear stage) compared with normal concrete. The RCA proved to have a high strain capacity,

which indicated high ductility. The maximum RCA strains ranged from 0.0056 to 0.0072, whereas the maximum NC strain was 0.0042.

Further, as can be seen from Figure 7, the cone-type failure mode in the cylinders appeared in NC and RCA concrete.

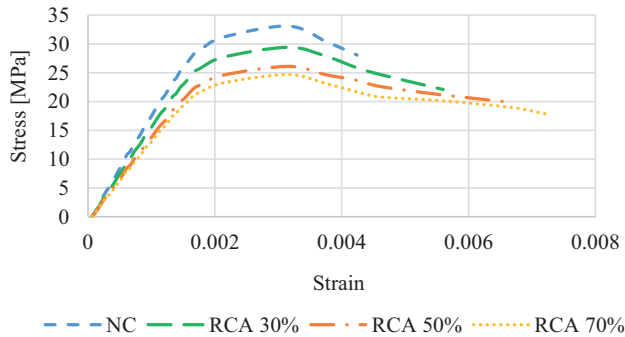


FIGURE 6. The stress–strain relations



FIGURE 7. Cylinders failure mode

Flexural strength

Concrete flexural strength is an indirect measure of tensile strength in flexure. Table 4 shows a slight decrease in the modulus of rupture compared with NC (18.83% decrease). According to Figure 8, all samples had a fracture in the middle third.

TABLE 4. Modulus of rupture (f_r)

Concrete mix	Modulus of rupture (f_r) [MPa]
NC	42.30
RCA 30%	38.45
RCA 50%	34.31
RCA 70%	32.75



FIGURE 8. Fracture position in concrete prisms

Splitting tensile strength

The tensile strength of concrete with RCA was lower, but less than that of the compressive strength, whereas the tensile strength drop-

ped from 5.126 to 4.582 $\text{N}\cdot\text{mm}^{-2}$ (10.61% decrease) in comparison to the normal concrete. The reason for this was that the surface of the RCA was rough due to residual mortar that provides good bonding strength with the concrete, unlike the case where the compression behaviour was weak. Table 5 shows the experimental indirect tensile strength (f_{cr}).

TABLE 5. Indirect tensile strength (f_{cr}) cylinder concrete according to tensile load (P_t)

Concrete mix	P_t [kN]	$f_{cr} = \frac{2P}{\pi DL}$ [$\text{N}\cdot\text{mm}^{-2}$]	$f_{cr} = 0.7\sqrt{f_{cu}}$ [$\text{N}\cdot\text{mm}^{-2}$]
NC	362.335	5.126	4.552
RCA 30%	352.086	4.981	4.340
RCA 50%	339.009	4.796	4.100
RCA 70%	328.882	4.582	4.005

The behaviour of reinforced beams in flexural tests

Crack patterns and failure modes

The crack patterns and failure modes of the beams were investigated. As shown in Figure 9, the RCA concrete beams exhibited more cracks at the initial cracking stage than the control beam. This phenomenon could be explained by the fact that the ITZ between the RCA and paste was weaker than the ITZ between the NA and paste. The RCA concrete's weak ITZ was caused by residual mortar on the surface of the RCA. New cracks appeared inside and outside the constant bending zone in both the NA and RCA beams as the load increased after the initial cracking stage. Both types of beam failed in flexure as a result of new and present cracks propagating up to the compression zone. The number of cracks in the RCA beams, on the other hand, was greater than in the control

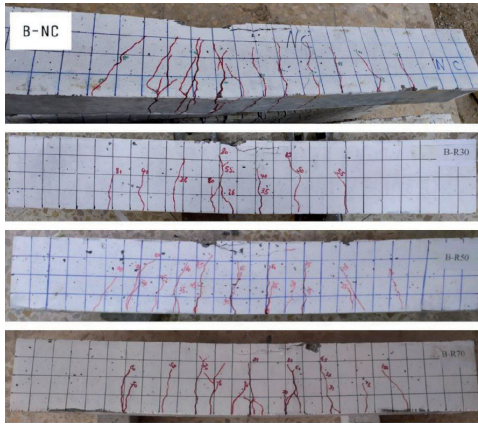


FIGURE 9. Typical crack patterns for beams

beam (B-NC). The test results revealed that tensile cracks developed first, followed by the yielding of the tensile rebar and concrete crushing, which is often identified as a tension failure. The first cracks developed on the beam’s bottom face, between the loading points, where it was exposed to pure bending. The cracks became larger as they progressed toward the upper face. Additional

flexural cracks occurred between the load and the supports as the load increased after the first cracking. As the applied load was increased more, most of the flexural cracks formed vertically, and slant flexure-shear cracks emerged.

Load–deflection relationships

The load–deflection curves of both NA and RCA beams are shown in Figure 10. In the initial cracking state, for all beams, the load–deflection relationships were linear and almost similar, while the deflections were proportional to the loads. It was noticeable that increasing the replacement by RCA led to reduced load-carrying capacity. The stiffness of the RCA beams decreased when the load was increased. When the load reached about 0.85–0.90% of the ultimate load, the load–deflection curves tended toward the horizontal axis. The RCA beam load–deflection curves showed greater ductility than the NC beam. It can be noted that the RCA beams had higher deflections than

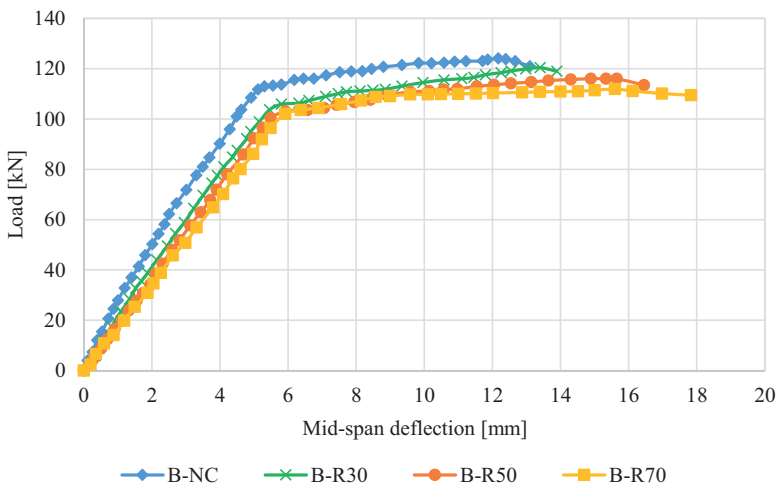


FIGURE 10. Load–deflection curve for beams

the NC beam. The increase in the deflections for beams with RCA replacement might be due to the lower modulus of elasticity of the RCA beams. Furthermore, the load values for RC beams at $\Delta_u = 12.17$ mm for the NC beam were 124.08 kN, 118.41 kN, 113.73 kN and 110.32 kN for B-NC, B-R30, B-R50 and B-R70 respectively.

Stages of loading and displacement

Table 6 summarises the substance of the experimental results. The cracking load (P_{cr}), yield load (P_y), ultimate load (P_u), and related mid-span deflection are essential backlashes of the flexure critical beam, which are obtained from the load–deflection relation of the tested specimens.

As for beams in which 30%, 50% and 70% of the NA has been replaced by RCA, the first cracking load was a decrease by about 20.67%, 28.5% and 38.3% respectively, in comparison with beam B-NC. The lower cracking load of the RCA beams was attributed to the weaker ITZ between the cement paste than in the NA beams. Similarly, the ultimate load was a decrease by about 3.0%, 6.5% and 10.5% respectively. This implies that when the RCA content increased, the flexural ultimate strength decreased.

Conclusions

The results described here suggest the following conclusions:

1. Replacement of normal aggregates (NA) in concrete mixes by recycled concrete aggregates (RCA) caused a decrease in the compressive strength for cubes by 9.10%, 18.88% and 22.57%, and a decrease in the compressive strength for cylinders by 10.87%, 20.9% and 25.21%, for replacement ratios of 30%, 50% and 70% respectively.
2. The stress–strain curve for RCA concrete cylinders showed a high strain capacity (high ductility) in comparison to normal concrete (NC).
3. The splitting tensile strength and flexural strength of RCA concrete decreased variously with the increasing proportion of recycled aggregate (10.61% decrease).
4. The RCA concrete showed a slight decrease in the modulus of rupture compared with NC (18.83% decrease).
5. The results expressed that the RCA beams had a higher number of cracks than the normal concrete beam. As a result of the cracking pattern, the RCA beams showed mostly closer crack spacing and less width than the NC beam.

TABLE 6. Summary of the test results of the beams

Beam	Initial cracking stage		Yielding stage		Ultimate stage		Mode of failure
	P_c [kN]	Δ_{cr} [mm]	P_y [kN]	Δ_y [mm]	P_u [kN]	Δ_u [mm]	
B-NC	35.8	1.10	115.5	6.2	124.08	12.17	flexure
B-R30	28.4	1.50	106.9	6.6	120.40	13.40	flexure
B-R50	25.6	1.25	103.3	6.5	116.08	15.65	flexure
B-R70	22.1	1.00	102.9	6.8	111.14	16.12	flexure

6. The deflection, first crack load, and ultimate load for RC beams decreased with the increasing replacement ratio of RCA.
7. The load-carrying capacity decreased by 2.96%, 6.47% and 10.42% at replacement ratios of 30%, 50% and 70% respectively.

Acknowledgements

The authors appreciate the materials laboratory of the College of Engineering, University of Thi-Qar (UTQ) for their assistance in the experimental work.

References

- ASTM International (2003). *Standard specification for concrete aggregates* (ASTM C33). West Conshohocken, PA.
- ASTM International (2015). *Portland cement standard specification* (ASTM C150/C150M). West Conshohocken, PA.
- ASTM International (2022). *Standard specification for deformed and plain carbon-steel bars for concrete reinforcement* (ASTM A615/A615M). West Conshohocken, PA.
- Boltryk, M., Małaszkiwicz, D. & Pawluczuk, E. (2007). Beton zwykły na kruszywie wtórnym – podstawowe właściwości techniczne [Concrete with recycled aggregate – basic technical properties]. *Zeszyty Naukowe Politechniki Białostockiej. Budownictwo*, 31, 65–73.
- Karlsson, M. (1998). *Reactivity in recycled concrete aggregate*. Göteborg: Chalmers University of Technology.
- Meddah, M. S., Al-Harthy, A. & A. Ismail, M. (2020). Recycled concrete aggregates and their influences on performances of low and normal strength concretes. *Buildings*, 10 (9), 167. <https://doi.org/10.3390/buildings10090167>

- Saadoon A. M., Mashrei M. A., Al Oumari K. A. (2022). Punching shear strength of recycled aggregate-steel fibrous concrete slabs with and without strengthening. *Advances in Structural Engineering*, 25 (10). <https://doi.org/10.1177/1369433222109028>
- Xiao, J., Li, W., Fan, Y. & Huang, X. (2012). An overview of study on recycled aggregate concrete in China (1996–2011). *Construction and Building Materials*, 31, 364–383.
- Yang, I. H., Park, J., Kim, K. C. & Lee, H. (2020). Structural behavior of concrete beams containing recycled coarse aggregates under flexure. *Advances in Materials Science and Engineering*, 2020, 8037131. <https://doi.org/10.1155/2020/8037131>

Summary

Mechanical properties and flexural behaviour of reinforced concrete beams containing recycled concrete aggregate. Increasing waste recycling has become an essential process in the construction industry due to the environmental and economic advantages, such as minimizing waste in landfills, saving natural resources, and decreasing pollution. Crushing and sieving waste from standard compression test cubes is used to produce the recycled concrete aggregate (RCA). A set of standard concrete cylinders, cubes, and beam specimens were made by utilizing coarse aggregate replacement ratios of 0%, 30%, 50% and 70%. At the day 28 stage, the specimens were tested to determine compressive strength, stress–strain relationship, splitting tensile strength, and flexural strength. In addition, four reinforced concrete (RC) beams were cast and tested under a four-point load to evaluate the flexural behaviour of RC beams with partial replacement of the natural aggregate with RCA. One was a natural aggregate (NA) control beam,

while the others had varying RCA ratios (30%, 50% and 70%). The results show that the compressive strength of RCA concrete with the replacement by 30%, 50% and 70% decreased by 9.10%, 18.88% and 22.57% respectively, in comparison to the compressive strength of normal concrete (NC). The RCA concrete showed a high strain capacity, which indicated high

ductility. The maximum RCA type strains ranged from 0.0056 to 0.0072. Concrete flexural strength showed a slight decrease in comparison to NC (18.83% decrease), where the tensile strength showed a 10.61% decrease in comparison to NC. As for RC beams, the load-carrying capacity decreased by 10.5% with increases in the replacement ratio.

Igor GAJDÁČ  <https://orcid.org/0000-0002-1315-2914>

Luboš KUČERA  <https://orcid.org/0000-0001-5232-7601>

Tomáš GAJDOŠÍK  <https://orcid.org/0000-0002-0622-2427>

Viera KONSTANTOVA   <https://orcid.org/0000-0003-3477-498X>

University of Žilina, Faculty of Mechanical Engineering, Slovakia

A REVIEW OF THE FACTORS AND INPUT PARAMETERS INFLUENCING THE RANGE OF AN EDISON ELECTRIC VEHICLE ACCORDING TO MEASUREMENTS

Key words: EV range, battery temperature, tyre condition, energy efficiency of the drive, acceleration, additional energy sources

Introduction

The increased global demand for electric vehicles (EVs) is due to an increase in the quality of life in cities. The EVs have almost zero carbon emissions (no exhaust emissions) and low noise in operation (Nanaki, 2021). The development of EVs was accelerated by the stricter tests of the Worldwide Harmonized Light Vehicle Test Procedure (WLTP).

However, the economic and environmental impact depends on the sources of electri-

cal energy used to charge the EV batteries (Kucukoglu, Dewil & Cattrysse, 2021). In addition, environmental responsibility is often suppressed by the driver's increased fear (Franke, Rauh & Krems, 2016; Kaviani-pour et al., 2021; Miri, Fotouhi & Ewin, 2021) of the EV's range. The fear of limited EV range is called range anxiety. Increasing the battery capacity or the number of charging stations is not enough for drivers to overcome their fear (Kavianipour et al., 2021; Miri et al., 2021). It is reported in Ozatay et al. (2014), Hong, Park and Chang (2016) that accurate estimation of the remaining range can effectively alleviate the concerns of drivers. Range estimation of the EV is one function of a technology

known as Energy Assistant (EA). The main function of EA is to inform drivers about the current range and how to avoid a critical situation while driving an EV.

It is known that battery capacity decreases over time due to an increase in internal resistance. The degradation of battery capacity causes significant problems with the efficiency and reliability of EVs (Vatanparvar & Faruque, 2017). Increasing or decreasing the range of the EV is directly related to energy consumption. Many factors can affect the energy consumption and range of an EV (Vatanparvar & Faruque, 2017; Xiong, 2020; Kucukoglu et al., 2021). Investigating these

factors and parameters that could affect the range and energy consumption of an EV is the focus of this paper.

The information presented in this article can be used for the next development of the EA algorithm for EVs in further experimental work. The aim of this article is to review the parameters and input data based on measurements performed with a small EV under real driving and laboratory conditions. In the next part of the text, the basic technical parameters of the vehicle and the measuring device are presented. Sources of the input data are summarily presented in the last part.

TABLE 1. Factors influencing the EV energy consumption

I. Vehicle design and construction	Influence on driving resistance	Rolling resistance	Vehicle weight	
			Tyre construction	
		Air resistance	Aerodynamically clean vehicle shape and size	
		Resistance from ascents	Vehicle weight	
		Inertia resistance	Vehicle weight	
	Inappropriate construction and structure of modules	Oversized total stored energy in the batteries		Weight of batteries
				Price of batteries
				Battery lifetime
				Space in the vehicle
		Incorrectly selected components		Recuperation system
			Insufficient performance	
		Minimum compatibility within the functionality of the system		
		Incompatibility with the operating environment of the electromechanical drive		
II. Operational condition			Heavy urban traffic	
			Road surface	
			Chosen route	
			Climatic conditions	
III. Driver subjective influence			Driving style	
			Preparation of the vehicle before driving	
			Use of vehicle electricity for non-traction purposes	
IV. Other energy sources			Recuperation	
			Photovoltaic panels	
			Other technical devices for extended range	

Source: own work.

Factors influencing the energy consumption and range of EVs

In general, the energy balance expresses the ratio of the amount of energy input to the amount of energy output. It indicates the ratio of electrical energy received and stored in the batteries of the EV and the mechanical energy converted in the electric motor for traction purposes. The real use of energy is influenced by several factors. All factors which influence the energy consumption in EVs and range are presented in Table 1.

Factor I. Vehicle design and construction. The most significant negative design parameter is the vehicle weight, which can be influenced during the vehicle design (Chen & Crolla, 2007; Hrček, Medvecký & Bisták, 2017). Parts of an electric power train replace those of conventional vehicles, such as voluminous cylinder blocks, crankshaft, and transmission (Weiss, Cloos & Helmers, 2020). The weight of the vehicle is influenced by the size of the battery (Weiss et al., 2020; Xiong, 2020). The solution is a multifunctional and modular vehicle concept using today's advanced manufacturing technologies (Habek, Lavios & Krupah, 2020; Schmid, Tomek & Hanus, 2022), cutting-edge electronic systems, new construction materials, and miniaturization in the field of components for vehicles with unconventional power sources. The oversized total stored energy affects the size of the battery box, which subsequently affects the curb weight and price of the vehicle (Chang, Baek & Hong, 2014; Redelbach, Özdemir & Friedrich, 2014). The correct size of the battery can extend the range. If an EV is used, for example, to commute to work and the daily route does not exceed 50 km, then the total battery capacity may be 24 kWh. The EV is then lighter and has lower energy

consumption (Münster, Schäffer, Kopp, Kopp & Friedrich, 2016). Nowadays, modular design is becoming a novel trend in helping to choose the appropriate size of the battery according to customer needs.

Factor II. Operational condition. The operational conditions can influence the driver's behaviour (Franke, Neumann, Buhler, Cocoron & Krems, 2012). For example, an intelligent traffic management system, such as a navigation system (Vatanparvar & Faruque, 2018), assists the driver in selecting the optimal route in heavy urban traffic. Next, the climatic conditions and the nature of the environment significantly affect the range of an EV. The range decreases at extremely low and high environmental temperatures (Lindgren & Lund, 2016; Vatanparvar & Faruque, 2018; Argue, 2021), and according to Vatanparvar and Faruque (2018) the optimal temperature for an EV is 21.5°C. Manufacturers attempt to limit this problem by using different cooling or heating systems for the batteries (Ji & Wang, 2013; Jaguemont, Boulon & Dubé, 2016; Geotab, 2021; MAHLE, 2021).

Factor III. Driver subjective influence. The driving style has a significant impact on the range of EVs. The drivers should adapt their driving habits to minimize unnecessary braking and acceleration, as well as other energy consuming modes. It is advantageous to use coasting, gliding or recuperation to convert kinetic energy into electrical energy during deceleration and braking. One way to influence the driving style is to use a system with a defined driving style. Before driving, the driver can reduce energy consumption by preparing the vehicle appropriately for driving, such as by removing any unnecessary load, checking the technical condition of the vehicle (pressure in the tyres, preparing an itinerary of the charging stations, and so

on). While driving, the driver can reduce the energy consumption by rational use of the vehicle's electrical equipment, such as air conditioning, heating and various comfort features.

Factor IV. Additional energy sources to extend the range. Based on the design capabilities of the vehicle and its operating environment, the driver can assess the possibility of using additional energy sources to extend the range. For example, the effectiveness of brake energy recovery (Hu et al., 2020), the use of photovoltaic panels (Dwibedi, Jayaprakash, Siva & Gopinath, 2020; Li, Yu & Feng, 2020) directly on the vehicle, the method, and the type of charging, etc. Concerning additional energy sources for the operation of the vehicle, it is important to note that an EV has zero CO₂ emission if it uses energy produced with zero CO₂ emissions during its lifetime (De Pinto et al., 2016). Solar energy affords a simple and elegant method, by using solar radiation to make energy available to EVs (Li et al., 2020).

Experimental Edison EV

A small Edison EV is a research student project designed at the University of Žilina. The Edison EV serves to gain new information and experience in the development,

construction, and operation of EVs and their infrastructure. The Edison EV project was carried out from conceptual design to a functional prototype. The technology used allows various settings, diagnostics, chassis and drive optimization, programming of control units, and monitoring of components for subsequent processing of the acquired data. Other uses of the vehicle include testing the EV infrastructure components, chargers, charging modes, vehicle motion monitoring, servicing, and diagnostics.

The Edison EV is a small urban two-seater EV (Fig. 1). The load-bearing part of the vehicle is a space-tube frame integrated into a single-space body. The drive is provided by an electric motor with a gearbox mounted in front of the rear axle, along with a programmable frequency converter to control it.

The technical specifications of the Edison EV are presented in Table 2. The electric drive of the vehicle consists of a three-phase asynchronous motor with a short armature. It is a maintenance-free and highly over-loadable electric motor originally designed for axle mounting similar to the smart EV. The Curtis frequency converter includes the control software. The two LiFeYPO₄ traction batteries have 25 cells, 300 Ah capacity, and 80 V traction voltage, along with battery management system (BMS) control unit and balancers. For the Edison EV it is possible



FIGURE 1. Design of the Edison EV, carried out at the University of Žilina (image credit: the authors)

TABLE 2. Technical specification of the Edison EV

Parameter	Value
Vehicle dimension (length / width / height) [mm]	3 100 / 1 600 / 1 700
Wheelbase (front / rear) [mm]	2130 / 1320
Tyre dimension [-]	165 / 65 R14
Consumption energy per 100 km [kWh]	11.0–14.7
Combined range of Edison EV [km]	150–200
Battery capacity / Charging time [kWh·h ⁻¹]	24 / 15
Curb weight [kg]	1 050
Weight per axle (front / rear) [kg]	520 / 530
Total weight [kg]	1300
Battery weight [kg]	250
Power of the electric motor (maximum / nominal) [kW]	30 / 15
Maximal speed [km·h ⁻¹]	90

Source: own work.

to use the 16 A/83 V on-board charger, and its parameters define the charging time. A BMS is an electronic system that controls the flow of energy while charging the batteries (Cieslik et al., 2021). The BMS monitors their state, recalculates the data and displays it. The BMS also manages the distribution of energy during charging and recuperation back to the batteries.

Measurement of selected factors and input parameters for the Edison EV

The measurements were carried out under real-life driving conditions. The dynamometer, a MAHA MSR 1050 Roller, was used for the laboratory test work (Commission Regulation (EC) 692/2008, Commission Regulation (EC) 2017/1151; Pavlovič, Ciuffo, Fontaras, Valverde & Marotta, 2018; Li, Wang, Wu, Tian & Tian, 2021). It is possible to perform complex

field research activities concerning the use of unconventional vehicle drive systems. The laboratory is involved in working with the organizations that form part of the E-Mobility platform. The laboratory is accredited, making it possible to perform measurements for legislative changes. Comprehensive testing of conventional vehicles with internal combustion engines, EVs, and unconventional vehicles is performed. A full description and the technical data for the testing are accessible on the web page: maha-france.fr.

On-board computers with an internal combustion engine after refuelling, and for EVs after charging the batteries, measure the fuel consumption (l per 100 km) or electricity consumption (kWh per 100 km). The range is continuously updated according to the amount of fuel in the tank or the remaining charge in the batteries.

The function of an EA not only determines the range of a vehicle, calculated as the difference between energy received and

TABLE 3. Source of input data for parameter factors, Part I

Climatic conditions	Monitored parameter	Source of input data	
		Installed in the EV	Laboratory measurement
Environment	Temperature	Sensor	–
Batteries	Temperature	BMS	–
	Discharge characteristic for different temperatures	–	✓
	State of charge	BMS and frequency converter	–
Technical condition of components	Monitored parameter	Source of input data	
		Installed in the EV	Laboratory measurement
Tyres	Design of tyres and effect on rolling resistance	–	✓
	Pressure in tyre and effect on rolling resistance	–	–
Batteries	Number of charging cycles	BMS	–
	Battery lifetime	–	–
Mechanical drive components	Energy transmission efficiency	–	✓
Electrical drive components	Temperature	Sensors	–

Source: own work.

TABLE 4. Source of input data for parameter factors, Part II

Driver subjective influence	Monitored parameter	Source of input data	
		Installed in the EV	Laboratory measurement
Route selection	GPS routes (3D maps)	✓	–
	Pressure in tyre and effect on rolling resistance	–	–
Driving style	Energy consumption converted into periodic intervals	–	✓
Dynamic driving parameters	Vehicle speed, lateral and longitudinal acceleration	Sensors	–
Vehicle drive	Drive efficiency map	–	✓
Energy sources	Monitored parameter	Source of input data	
		Installed in the EV	Laboratory measurement
Batteries	Energy	BMS	–
Brake recuperation	Energy	BMS	–
Photovoltaic panels	Energy	BMS	–
Range extender	Energy	BMS	–
Charging station	GPS (3D maps)	–	–

Source: own work.

consumed. The EA helps, controls, manages, updates, and communicates with the driver. The EA informs the driver about the risk of discharging the batteries, before reaching a charging station, and suggests precautions to ensure that the driver stops at the nearest charger. The EA performs tasks before and during the entire drive to the charging station. An investigation of the factor parameters is summarized in Tables 3 and 4.

Results and discussion

Operating an EV at low temperatures has the effect of increasing energy consumption, which means a shorter range. “Self-heating” the batteries in our experimental Edison EV with a total stored energy of 24 kWh reduces the range by 7–10 km. The EA could correct the range value before driving based on battery temperature data and the discharge characteristic for different EA temperatures. It would limit the energy from recuperation, limiting the maximum power output of the electric motor. If the Edison EV allowed fast charging, EA would limit the maximum charging current, all with the sole purpose of protecting undercooled batteries from high currents. Low temperatures reduce the performance of the batteries due to increased internal resistance and can also damage them. However, the increased resistance accelerates the heating of the accumulators. The Edison EV has LiFeYPO₄ batteries with a capacity of 300 Ah and a traction voltage of 80 V. Low temperatures reduce the performance of the batteries while the energy consumption for heating shortens the range.

The Edison EV was parked for several days at sub-zero temperatures while at the same time consumption measurements were performed. The comparison with the

latest consumption confirmed that by gradual warming of the batteries, electricity consumption decreases. At the beginning of the measurements, the consumption was 18.5 kWh per 100 km, and then after warming was up to 14.9 kWh per 100 km. For a better comparison, three cases were selected where the vehicle needed the same 10.4 kW of power from its batteries. In the first case, the batteries were cold at start-up, and then in the second case the cells were heated because the batteries were charged for 10 km of driving. In the first and second cases, the ambient temperature was 0°C. In the third case, the ambient temperature was 18°C. At low temperatures the increased internal resistance caused a significant voltage drop, i.e., the EV in winter at the same power consumed more current from the batteries.

The Edison EV does not feature a battery heating system. Producers attempt to heat the batteries, such as by a battery heating system or by the heat emitted by an electric motor, which is an efficient solution because it does not use the energy of the batteries (Jaguemont et al., 2016). We analysed the possibilities of using heat-to-heat batteries. Temperatures of the Edison electric motor and converter were recorded for eight cycles lasting 1.5 h. The ambient temperature was 0°C. The EV drove 14 km, the temperature of the electric motor was 74°C and the converter temperature was 46°C at the end of the run.

The degree of influence of the technical parameters of the tyres on the energy balance of an EV on the range is crucial for the development of an EA. The monitoring of electricity consumption was carried out under different driving and load modes by the Edison EV in a stable laboratory environment, with the elimination of the subjective influence of the driver.

Selected technical parameters of vehicle tyres were divided according to the type, into summer and winter sets of tyres, and in terms of operating conditions as tyres inflated to the prescribed pressure and to an under-inflated pressure. While the driver is not influencing the construction of the tyre, he is responsible for taking care of the condition of the tyres. Underinflated tyres negatively affect not only the energy consumption and range, but also the safety of the vehicle.

The Edison EV with tyres set to the prescribed pressure travelled a distance of 147 m during deceleration from an initial speed of $30 \text{ km}\cdot\text{h}^{-1}$ to a stop. For low-pressure tyres, the distance averaged 118 m. The deceleration difference between low and prescribed tyre pressure was 29 m. The deceleration from a speed of $50 \text{ km}\cdot\text{h}^{-1}$ was an average difference of 59 m.

The WLTP test was performed in laboratory conditions. Under defined measurement conditions the methodology allows the simulation of realistic driving characteristics for the vehicle. Despite the speed limit of the Edison measuring vehicle being up to $90 \text{ km}\cdot\text{h}^{-1}$, three of the four-speed phases were implemented on the measuring device, each phase having several braking, stopping, and acceleration modes according to the track profile. The results demonstrated that if the vehicle travelled an average distance of 10.77 km, the electricity consumption per 100 km was on average 16.795 kWh per 100 km for underinflated tyres and 16.08 kWh per 100 km for correctly-inflated tyres. This means that underinflated tyres have a 4.26% higher consumption. In real-life conditions, consumption can be even higher because of the subjective influence on the driver, natural conditions, and various other situations.

An important parameter in monitoring the electricity consumption of an EV is the energy efficiency of energy transfer from batteries to the drive wheels. Therefore, the aim was to determine the drive mode in the area with the best efficiency to thus optimize the driving style. The vision was that the EA would inform the driver based on the drive efficiency map and real-time data, such as speed and battery performance. A decisive part of Edison EV driving takes place in a mode that corresponds to the map of the area with lower efficiency.

The Edison EV, like most EVs, has a single-speed planetary gearbox. Due to this, the movement of the vehicle in the higher efficiency area is limited. The gear ratio of the gearbox is designed so that the entire drive provides the required dynamic parameters. The advantage of an EV is that it allows kinetic energy to be recovered during braking, which is highly convenient in urban traffic. On the other hand, the most effective option is to use deceleration. Based on the analysis and measurement of the acceleration, at higher acceleration, the energy consumption is identical to that at low acceleration. There was the possibility to increase the efficiency of the Edison EV by developing a special driving style.

This driving style assumed that a longer period of favourable energy efficiency of the idle wheels would compensate for higher acceleration. The driving style was designed for urban transport, which means that the speed was usually $50 \text{ km}\cdot\text{h}^{-1}$. The up-down cycle used acceleration from 45 to $55 \text{ km}\cdot\text{h}^{-1}$ and maintained a deceleration mode from 55 to $45 \text{ km}\cdot\text{h}^{-1}$. Although there was a difference between stable driving and this driving style, the drive would operate more efficiently during the up-down cycle.

The vehicle must overcome higher driving resistances, but energy consumption will be zero if it is coasting. This is an advantage of an EV over a conventionally powered vehicle with an internal combustion engine. The up-down driving cycle was compared with the stable driving cycle. The distance and time were identical in both cycles, and the distance was 2.4 km. The energy consumption of the batteries was 0.33 kWh for both the up-down driving cycle and the stable driving cycle. The situation was different in the field of energy, which was measured on the tyres.

The up-down cycle was more energy intensive than stable driving, and measurements confirmed this finding. The average energy required to complete the up-down cycle was 0.21 kWh, while at stable speed the energy required was 0.17 kWh. It shows that the vehicle needed more energy to overcome the rolling resistance during the up-down cycle. The total energy consumption was identical for both driving cycles. The efficiency of the drive system was 62% with the up-down cycle, more than a 10% difference compared to a stable driving cycle. The energy consumed by the batteries was identical in both cases. Using the up-down driving style was not useful in normal traffic because it did not extend the range of the vehicle.

The number of planned stops, traffic density, and charging station network specified in the selected route influenced the EV range as well. The usable input value would be more accurate if intelligent traffic management data was available. The EA would be able to correct the range value based on a database of available digital maps.

Driving style is a purely subjective indicator of the influence of the driver. From the point of view of energy consumption, it is more advantageous to slow down by coasting rather than braking when entering

a village or at an intersection. For maximum use of the kinetic energy at the right time in order to reduce speed or come to a complete stop if the traffic situation requires it. The route profile and traffic situation, the weight and speed of the vehicle, the recuperation effect, and the database of measured data can comprise several main input parameters for the decision-making process of the EA system, which can communicate with the driver by visual or audio signals. The aim is to provide the driver with information on how to achieve the lowest electricity consumption.

Acceleration is another subjective parameter of driving style, as it is more energy intensive than a smooth ride. By a suitable combination of the time required to travel a certain distance and by mapping the overall efficiency of the electric drive, it is possible to optimize the acceleration of the motor. Using the map of the overall efficiency of the drive, the EA can decide and inform the driver whether he is in the most efficient mode at the beginning of the acceleration – in the highest efficiency mode. Suppose a driver has to accelerate from an intersection. The system uses GPS position to evaluate the final speed during acceleration to $50 \text{ km}\cdot\text{h}^{-1}$. Based on the drive efficiency map, the system can inform the driver by a graphical display on the instrument panel which acceleration mode should be selected, fast or slow. The system can help the driver achieve the optimal mode.

An analysis of three types of acceleration from 0 to $50 \text{ km}\cdot\text{h}^{-1}$ was performed. The distance travelled was 200 m under all three accelerations. The first acceleration lasted 27 s, the second acceleration was 22 s, and the third acceleration was 19 s. Five measurements were performed for each acceleration test. The average energy consumption

was 0.069 kWh for the first acceleration, 0.072 kWh for the second acceleration, and 0.072 kWh for the third acceleration. The measurements indicated that the Edison EV had almost the same energy consumption for slow and fast accelerations. Although the vehicle overcomes higher driving resistances at fast acceleration, this compensates for the overall higher efficiency of the drive at higher loads. During deceleration, it is more efficient to use deceleration and then recovery. The disadvantage of driving is the longer deceleration time, which that is compensated by faster acceleration. Energy consumption is not affected due to the efficiency of the Edison EV.

Updating the number of kilometres travelled requires continuous monitoring of electricity consumption. The monitoring has three primary indicators: operational (under which conditions the vehicle is driven), the subjective influence of the driver (driving style), the use of other equipment (vehicle lighting, heating) or the use of energy sources (energy recovery, photovoltaic panels). The EA can update the number of kilometres travelled according to the current value of the energy stored in the traction batteries (SOC) and the monitoring of the energy consumption mode. This is not a final value, because if the EA works with data on the current route of the EV, the value continues to be recalculated. The relationship between the discharge characteristics of the traction batteries used and the capacity drop was measured in the areas of 80% SOC and 20% SOC, with a direct effect on the range of the Edison EV.

In conclusion, the EV driver does not directly support the control and protection of the electrical components. The continuing healthy condition of all the electrical components is required for the correct EA

function. The EA must control all the appliances in the vehicle, including the ability to switch off selected systems to allow the driver to adapt the driving style and control the conversion of electrical energy into traction energy. It is not directly controlled by their condition. The protection of electrical components is the task of the EA, such as at low and high battery temperatures, the electric motor, and the converter. What is important is the communication between the EA and the driver, such as through the communication panel. Using audio-visual communication, the EA can help the driver to optimize their driving style and minimize energy consumption. Modern components in the EV can collect a wide range of parameters, and therefore it is possible to change the set parameters and to monitor their impact on energy consumption. The data measured under real conditions can be verified on a cylinder dynamometer.

Conclusions

According to the conducted surveys, 60–65% of customers interested in buying an EV are afraid of the short range and the lack of availability of charging options. The Energy Assistant (EA) is one of the tools to eliminate the stress and concerns of customers by assisting and realistically evaluating the current drive or the conditions of the required range. It assists even before driving, when it evaluates the effect of temperature on battery discharge, during driving and in the event of a crisis situation, when the expected driving distance is shorter than the distance to the nearest charging station. The EA needs data for their decision-making. The data is the subject of the research description. Research is still ongoing and the data is constantly

being supplemented. Supplementing the data improves the EA's ability to more accurately evaluate the range of the electric car. The research can be further used for autonomous vehicles, as the autonomous driving system can be configured in such a way that the EV operates in an optimal mode for energy consumption.

Acknowledgements

The article was written with support of project APVV-18-0457 – Special Light Electric Vehicle from Un-conventional Materials to Heavy Conditions and Terrain – LEV.

References

- Argue, Ch. (2020). *To what degree does temperature impact EV range?* Retrieved from: <https://www.geotab.com/blog/ev-range> [accessed 27.10.2021].
- Chang, N., Baek, D. & Hong, J. (2014). Power consumption characterization, modeling and estimation of electric vehicles. In *2014 IEEE/ACM International Conference on Computer-Aided Design (ICCAD)*, San Jose, CA, USA, 2–6 November 2014 (pp. 175–182). <https://doi.org/10.1109/ICCAD.2014.7001349>
- Chen, D. C. & Crolla, D. A. (2007). Subjective and objective measures of vehicle handling: drivers & experiments. *International Journal of Vehicle Mechanics and Mobility*, 29 (S1), 576–597. <https://doi.org/10.1080/00423119808969588>
- Cieslik, W., Szwajca, F., Zawartowski, J., Pietrzak, K., Rosolski, S., Szkarlat, K. & Rutkowski, M. (2021). Capabilities of nearly zero energy building (nZEB) electricity generation to charge electric vehicle (EV) operating in real driving conditions (RDC). *Energies*, 14 (22), 7591. <https://doi.org/10.3390/en14227591>
- Commission Regulation (EC) No 692/2008 of 18 July 2008 implementing and amending Regulation (EC) No 715/2007 of the European Parliament and of the Council on type-approval of motor vehicles with respect to emissions from light passenger and commercial vehicles (Euro 5 and Euro 6) and on access to vehicle repair and maintenance information. OJ L 199, 28.7.2008, p. 1.
- Commission Regulation (EU) 2017/1151 of 1 June 2017 supplementing Regulation (EC) No 715/2007 of the European Parliament and of the Council on type-approval of motor vehicles with respect to emissions from light passenger and commercial vehicles (Euro 5 and Euro 6) and on access to vehicle repair and maintenance information, amending Directive 2007/46/EC of the European Parliament and of the Council, Commission Regulation (EC) No 692/2008 and Commission Regulation (EU) No 1230/2012 and repealing Commission Regulation (EC) No 692/2008. C/2017/3521. OJ L 175, 7.7.2017, p. 1.
- De Pinto, S., Lu, Q., Camocardi, P., Chatzikomis, Ch., Sorniotti, A., Ragonese, D., Iuzzolino, G., Perlo, P. & Lekakou, C. (2016). Electric vehicle driving range extension using photovoltaic panels. In *IEEE Vehicle Power and Propulsion Conference (VPPC)*, Hangzhou, China, 17–20 October 2016 (pp. 1–6). Piscataway Township: IEEE. <https://doi.org/10.1109/VPPC.2016.7791674>
- Dwibedi, R. K., Jayaprakash, R., Siva, T. & Gopinath, N. P. (2020). Hybrid electric vehicle using photovoltaic panel and chemical battery. *Materials Today: Proceedings*, 33, 4713–4718. <https://doi.org/10.1016/j.matpr.2020.08.351>
- Franke, T., Neumann, I., Buhler, F., Cocoron, P. & Krems, J. F. (2012) Experiencing range in an electric vehicle – understanding psychological barriers. *Applied Psychology*, 61 (3), 368–391. <https://doi.org/10.1111/j.1464-0597.2011.00474.x>
- Franke, T., Rauh, N. & Krems, J. F. (2016). Individual differences in BEV drivers' range stress during first encounter of a critical range situation. *Applied Ergonomics*, 57, 28–35. <https://doi.org/10.1016/j.apergo.2015.09.010>
- Geotab (2021). *Temperature tool for EV range*. Retrieved from: <https://www.geotab.com/fleet-management-solutions/ev-temperature-tool> [accessed 27.10.2021].

- Habek, P., Lavios, J. & Krupah, E. (2022). How car producers are driving toward sustainable supplier development. *Production Engineering Archives*, 28 (3) 268–278. <https://doi.org/10.30657/pea.2022.28.33>
- Hong, J., Park S. & Chang, N. (2016). Accurate remaining range estimation for electric vehicles. In *21st Asia and South Pacific Design Automation Conference (ASP-DAC)*, Macao, China, 25–28 January 2016 (pp. 781–786). Piscataway Township: IEEE. <https://doi.org/10.1109/ASPDAC.2016.7428106>
- Hrček, S., Medvecký, Š. & Bisták, M. (2017). Axle weighing system. In *Proceedings of the 58th International Conference of Machine Design Departments*, Prague, Czech Republic, 6–8 September 2017 (pp. 36–39). Prague: Czech University of Life Science. Retrieved from: http://2017.icmd.cz/proceedings/7_ICMD.pdf [accessed 27.10.2021].
- Hu, X., Zheng, Y., Howey, D. A., Perez, H., Foley, A. & Pecht, M. (2020). Battery warm-up methodologies at subzero temperatures for automotive applications: recent advances and perspectives. *Progress in Energy and Combustion Science*, 77, 100806. <https://doi.org/10.1016/j.pecs.2019.100806>
- Jaguemont, J., Boulon, L. & Dubé, Y. (2016). A comprehensive review of lithium-ion batteries used in hybrid and electric vehicles at cold temperatures. *Applied Energy*, 164, 99–114. <https://doi.org/10.1016/j.apenergy.2015.11.034>
- Ji, Y. & Wang Ch. Y. (2013). Heating strategies for Li-ion batteries operated from subzero temperatures. *Electrochimica Acta*, 107, 664–674. <https://doi.org/10.1016/j.electacta.2013.03.147>
- Kavianipour, M., Fakhrmoosavi, F., Singh, H., Ghamami, M., Zockaie, A., Ouyang, Y. & Jackson, R. (2021). Electric vehicle fast charging infrastructure planning in urban networks considering daily travel and charging behavior. *Transportation Research Part D: Transport and Environment*, 93, 102769. <https://doi.org/10.1016/j.trd.2021.102769>
- Kucukoglu, I., Dewil, R. & Cattrysse, D. (2021). The electric vehicle routing problem and its variations: a literature review. *Computers & Industrial Engineering*, 161, 107650. <https://doi.org/10.1016/j.cie.2021.107650>
- Li, S., Yu, B. & Feng, X. (2020). Research on braking energy recovery strategy of electric vehicle based on ECE regulation and I curve. *Science Progress*, 103 (1), 1–17. <https://doi.org/10.1177/0036850419877762>
- Li, X., Wang, T., Wu, C., Tian, J. & Tian, Y. (2021). Battery pack state of health prediction based on the electric vehicle management platform data. *World Electric Vehicle Journal*, 12 (4), 204. <https://doi.org/10.3390/wevj12040204>
- Lindgren, J. & Lund, P. D. (2016). Effect of extreme temperatures on battery charging and performance of electric vehicles. *Journal of Power Sources*, 328, 37–45. <https://doi.org/10.1016/j.jpowsour.2016.07.038>
- MAHLE (2021). *MAHLE develops new battery cooling system for faster charging of electric cars* (Press release 07.09.2021 Stuttgart). Retrieved from: <https://www.mahle.com/en/news-and-press/press-releases/mahle-develops-new-battery-cooling-system-for-faster-charging-of-electric-cars-85120> [accessed 02.10.2021].
- Miri, I., Fotouhi, A. & Ewin, N. (2021). Electric vehicle energy consumption modelling and estimation – a case study. *International Journal of Energy Research*, 45 (1), 501–520. <https://doi.org/10.1002/er.5700>
- Münster, M., Schäffer, M., Kopp, G., Kopp, G. & Friedrich, H. E. (2016). New approach for a comprehensive method for urban vehicle concepts with electric powertrain and their necessary vehicle structures. *Transportation Research Procedia*, 14, 3686–3695. <https://doi.org/10.1016/j.trpro.2016.05.487>
- Nanaki, E. A. (2021). Electric vehicles. *Electric vehicles for smart cities, trends, challenges, and opportunities* (pp. 13–49). Amsterdam: Elsevier. <https://doi.org/10.1016/B978-0-12-815801-2.00006-X>
- Ozatay, E., Onori, S., Wollaeger, J., Ozguner, U., Rizzoni, R., Filev, D., Michelini, J. & Di Cairano, S. (2014). Cloud-based velocity profile optimization for everyday driving: a dynamic-programming-based solution. *IEEE Transactions on Intelligent Transportation Systems*, 15 (6), 2491–2505. <https://doi.org/10.1109/TITS.2014.2319812>
- Pavlovič, J., Ciuffo, B. Fontaras, G., Valverde, V. & Marotta, A. (2018). How much difference

- in type-approval CO₂ emissions from passenger cars in Europe can be expected from changing to the new test procedure (NEDC vs. WLTP)? *Transportation Research Part A: Policy and Practice*, 111, 136–147. <https://doi.org/10.1016/j.tra.2018.02.002>
- Redelbach, M., Özdemir, E. D. & Friedrich, H. E. (2014). Optimizing battery sizes of plug-in hybrid and extended range electric vehicles for different user types. *Energy Policy*, 73, 158–168. <https://doi.org/10.1016/j.enpol.2014.05.052>
- Schmid, M., Tomek, P. & Hanus, P. (2022). Multi-physical contact simulation in vehicle applications. *Production Engineering Archives*, 28 (4) 369–374. <https://doi.org/10.30657/pea.2022.28.45>
- Vatanparvar, K. & Faruque, M. A. A. (2017). Electric vehicle optimized charge and drive management. *ACM Transactions on Design Automation of Electronic Systems (TODAES)*, 23 (1), 1–25. <https://doi.org/10.1145/3084686>
- Vatanparvar, K. & Faruque, M. A. A. (2018). Design and analysis of battery-aware automotive climate control for electric vehicles. *ACM Transactions on Embedded Computing Systems (TECS)*, 17 (4), 1–22. <https://doi.org/10.1145/3203408>
- Weiss, M., Cloos, K. C. & Helmers, E. (2020). Energy efficiency trade-offs in small to large electric vehicles. *Environmental Sciences Europe*, 32 (1), 1–17. <https://doi.org/10.1186/s12302-020-00307-8>
- Xiong, R. (2020). *Battery management algorithm for electric vehicles*. Singapore: Springer. <https://doi.org/10.1007/978-981-15-0248-4>

Summary

A review of the factors and input parameters influencing the range of an Edison electric vehicle according to measurements. Research and development help to improve the reliability of an EVs range, battery capacity, and trouble-free charging (or service). These factors affect the consumers' interest in EVs. The quality of EV use can be supported by a modern technology called Energy Assistant (EA). The task of EA is to inform the driver about the current range, the necessity to recharge the batteries, and so on to avoid a critical situation. The main aim of this article was to investigate factors and input parameters for the proposal of an EA. The Edison EV, designed at the University of Žilina, was used for experimental work under real conditions and in an accredited lab with MAHA equipment.

Wojciech CIEŹKOWSKI¹✉

Magdalena FRAK¹

Ignacy KARDEL¹

Marcin KOŚCIELNY²

Jarosław CHORMAŃSKI¹

¹ Warsaw University of Life Sciences – SGGW, Institute of Environmental Engineering, Poland

² Air-Concept Ltd Co., Poland

LONG-TERM WATER QUALITY MONITORING USING SENTINEL-2 DATA, GŁUSZYŃSKIE LAKE CASE STUDY

Key words: Sentinel-2, inland water, biological oxygen demand (*BOD*), dissolved organic carbon (*DOC*), electrical conductivity (*EC*), chlorophyll concentration (*CHL*)

Introduction

Water quality can be indicated by its physical, chemical and biological properties. Traditional water monitoring requires collecting samples in the field and analysing them in the laboratory. Although this in-situ measurement system offers high accuracy, it is a labour intensive and time-consuming process, and hence it is not feasible for providing a simultaneous water quality database

on a regional scale (Duan et al., 2013a; Duan et al., 2013b). Traditional monitoring methods are not easily able to identify the spatial or temporal variations in water quality, which is crucial for the comprehensive assessment of inland reservoirs (Gholizadeh, Melesse & Reddi, 2016). Traditional data collection systems are only able to represent point estimates of the quality of water conditions in time and space, and obtaining the spatial and temporal variations of quality indices in large waterbodies is almost impossible (Ritchie, Zimba & Everitt, 2003). Other disadvantages of in-situ monitoring include: (i) cost and time of field and laboratory work; (ii) monitoring, forecasting, and management of the entire waterbody may be impossible due to its

inaccessibility, such as due to the topography; and (iii) accuracy and precision of the collected in-situ data may be questionable due to both field-sampling errors and laboratory errors (Gholizadeh et al., 2016).

In recent decades, due to advances in space science and computer development, remote sensing techniques have begun to be used in wide environmental applications, such as in water quality monitoring. Remote sensing techniques make it possible to monitor water reservoirs on spatial and temporal scales unattainable by traditional monitoring. Since the 1970's, remote sensing techniques have been used for water quality assessment (Morel & Prieur, 1977; Brando & Dekker, 2003; Ritchie et al., 2003; Hadjimitsis & Clayton, 2009).

For the past four decades, remote sensing techniques have shown their strong capabilities in monitoring the quality of inland waters. Visible and near infrared regions of the spectrum are typically using by researchers to obtain robust correlations between reflectance and the physical, chemical and biological properties of water. Parameters like transparency (Kloiber, Brezonik, Olmanson & Bauer, 2002), chlorophyll concentration, i.e., phytoplankton (Gitelson et al., 2008), organic matter and mineral suspended sediments have been estimated by researchers in different waterbodies (Mancino, Nolè, Urbano, Amato & Ferrara, 2009; Giardino et al., 2014). Although the capabilities of remote sensing in assessing water quality are undeniable, this technique alone is not sufficiently precise and must be used in conjunction with traditional sampling methods and field surveying. With this in mind, the main advantages of water monitoring using remote sensing techniques are: (i) comprehensive views of entire waterbodies;

(ii) higher spatial and temporal scale of observations; (iii) possibility of synchronized monitoring of lake groups over a vast region; and (iv) comprehensive historical recording of water quality in an area and the possibility of trend analyses.

This paper focuses on applying existing empiric formulas to water quality estimation of Głuszyńskie Lake, located in the central Poland. Data from Sentinel-2 has been recorded since its launch in 2015, and has been used for estimating spatial and temporal changes in selected water quality parameters. The results were validated based on two field measurement campaigns (in 2021 and 2022). The aim of this work was to analyse whether existing empiric formulas could be applied for long-term quasi-continuous monitoring of inland waters in Poland, based on remote sensing data.

Material and methods

Study site

The study was conducted in Głuszyńskie Lake, central Poland. Głuszyńskie Lake is located near Radziejów, in the Kujawskie Lake District, part of the Kujawsko-Pomorskie Voivodship (Fig. 1), and it the largest reservoir in this region. It is a typical gutter lake, stretching along a north-south line, with two bays on the east and west sides. The lake is the deepest in the central part of the western bay. The lake is located in the upper part of the river basin of the Zgłowiączka river, where intensive farming is carried out. The lake is situated in one of the most intensively used agricultural areas in Poland and,

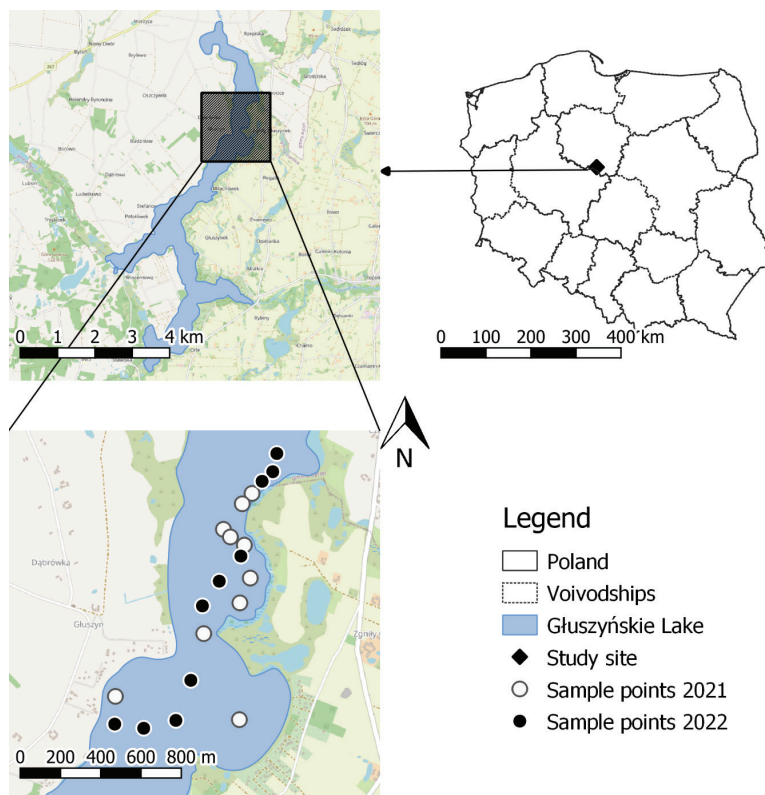


FIGURE 1. Study site location in Poland and water sample point locations in 2021 and 2022
Source: own studies (background map © OpenStreetMap).

consequently, the lake undergoes pollution from agriculture sources, especially in the northern part of the lake catchment area. Głuszyńskie Lake is part of in the State Environmental Monitoring of Surface Water process. Based on the monitoring results, high nitrate concentrations were identified during the spring and after intensive rains in the northern part of the lake. Currently, over 50% of the shoreline is occupied by recreational areas, including holiday cottages. This creates a threat to the water quality of the lake, as these develop without any legal or formal regulations for water and sewage management.

Water quality parameter calculations

For long-term spatial monitoring of the Głuszyńskie Lake the following water quality parameters were involved: biological oxygen demand (*BOD*), dissolved organic carbon (*DOC*), chlorophyll concentration (*CHL*) and electrical conductivity (*EC*). All values were estimated based on Sentinel-2 multispectral satellite images. Sentinel-2 LIC products with a relatively low cloud cover (less than 20%) were directly downloaded from Open Access Hub (<https://scihub.copernicus.eu/dhus/#/home>), dating back to its launch date on 23 June 2015 to 5 August 2022. Only the

images acquired during the growing season (from May to early October) were used. A total of 70 images were used for further analyses. The lake coastline was acquired from Map of the Hydrographic Division of Poland (downloadable by QGIS “Wody Polskie – Baza WMS” plugin by Ścisłowski, Państwowe Gospodarstwo Wodne Wody Polskie – KZGW & Wydział SIGW, 2022), and a 10 m inner buffer was created to exclude mixed pixels.

Typically, the formulas used for water quality parameters required bottom-of-atmosphere (BOA) reflectance. Hence, Sentinel-2 L1C were pre-processed to BOA reflectance using the `sen2r` R package (Ranghetti, Boschetti, Nutini & Busetto, 2020) using the R programming language (R Core Team, 2021).

In the scope of the analyses, a number of different formulas found in the literature were tested (results not shown). Selection of the calculation formulas used in the study was based on geographical rules. We selected equations which had been validated in Poland, the Baltic sea basin and central Europe, or tested in the world at a similar geographical latitude. We also limited the selection of formulas to those used only for inland lakes, excluding many formulas calibrated for oceans and seas. We finally selected the following formulas which gave the most promising results:

$$BOD = -141.51 \cdot \frac{(B4 - B5)}{(B4 + B5)} + 39.62 \quad (\text{Ślapińska, Berezowski, Frąk \& Chormański, 2016}), \quad (1)$$

$$DOC = 432 \cdot e^{-2.24 \cdot \frac{B3}{B4}} \quad (\text{Potes et al., 2018}), \quad (2)$$

$$CHL = 75.821 \cdot \frac{B5}{B4} - 42.644 \quad (\text{Osińska-Skotak, 2010}), \quad (3)$$

$$EC = 0.1252 \cdot \left[\left(\frac{B11}{B8} \cdot B12 \right)^2 + 4.1531 \cdot \left(\frac{B11}{B8} \cdot B12 \right) \right] + 10.527 \quad (\text{Abdelmalik, 2018}), \quad (4)$$

where BN is BOA reflectance in the Sentinel-2 N band.

Field and laboratory measurements

The validation of satellite-based water quality parameters were performed based on water samples (stored in two polypropylene containers: 60 ml and 1,500 ml) acquired from the top layer of the water on 8 October 2021 and 10 August 2022 in a total of 20 locations in the northern part of the lake (Fig. 1). The containers were transported to the laboratory by refrigerator and analysed on the same day. Point coordinates were recorded using a hand-held GPS unit with a measurement accuracy of 5 m.

In the field, *EC* was measured using a YSI Professional Plus probe (YSI Inc., USA), and the *CHL* was determined according the PN-ISO 10260 standard (Polski Komitet Normalizacyjny [PKN], 2002).

The biochemical oxygen demand (*BOD*) was determined using a volumetric method with a OxiTop® Control (WTW Ltd, Poland).

The analysis of dissolved organic carbon (*DOC*) concentration used a Formacs^{HT/TN} (Skalar Analytical B.V., Netherlands) – in compliance with the ISO 8245 standard (International Organization for Standardization [ISO], 1999) and EPA Method 415.1 (U.S. Environmental Protection Agency [EPA], 1983) – fitted with a platinum/cobalt column.

Before the analysis of these water samples they were filtered using 0.45 μm filters. The *DOC* determination was conducted with a high temperature catalytic oxidation method at 850°C (samples were acidified with HCl, mixed and aerated for 1 min immediately before the determination), according to the method recommended by the manufacturer.

Results and discussion

The highest mean values (higher than 50 $\text{mg O}_2\cdot\text{l}^{-1}$) of *BOD* were observed on 20 August 2015, 22 July 2016, 11 August 2018, 22 June 2019, and 1 July 2020 (Fig. 2). On 1 July 2020 a higher spatial variability (from 9.5 to 123.6 $\text{mg O}_2\cdot\text{l}^{-1}$) of *BOD* was observed. The highest yearly mean value (41.7 $\text{mg O}_2\cdot\text{l}^{-1}$) was observed in 2015 and the lowest (31.4 $\text{mg O}_2\cdot\text{l}^{-1}$) in 2017 (Table 1). These results show low variability in the mean values of *BOD* (both yearly and between all images) simultaneously with high spatial variability indicated by the bars in Figure 2.

The highest mean values (higher than 25 $\text{mg}\cdot\text{l}^{-1}$) of *DOC* were observed for nearly all images in 2022 (besides the last one acquired on 5 August 2022), and in this year the lowest spatial variability of *DOC* was observed. In the other years, only three times (16 July 2017, 10 September 2018 and 20 May 2020) were the mean *DOC* values higher than 25 $\text{mg}\cdot\text{l}^{-1}$ (Fig. 3). The highest yearly mean value (28.9 $\text{mg}\cdot\text{l}^{-1}$) was observed in 2022 and the lowest (11.5 $\text{mg}\cdot\text{l}^{-1}$) in 2016 (Table 1).

Mean *CHL* values varied between 50 and 75 $\text{mg}\cdot\text{m}^{-3}$ for the majority of the images. Only once (10 July 2017) was the mean *CHL* value higher than 75 $\text{mg}\cdot\text{m}^{-3}$ and reached

80 $\text{mg}\cdot\text{m}^{-3}$ (Fig. 4). In 2022 the mean *CHL* values was lower than 50 $\text{mg}\cdot\text{m}^{-3}$ (Fig. 4), and the yearly value in this year was also the lowest (36.2 $\text{mg}\cdot\text{m}^{-3}$). The highest yearly value of *CHL* (62 $\text{mg}\cdot\text{m}^{-3}$) was observed in 2017 (Table 1).

TABLE 1. Yearly mean values based on all cloud-free pixels within Głuszyńskie Lake of estimated water quality parameters

Year	<i>BOD</i> [$\text{mg O}_2\cdot\text{l}^{-1}$]	<i>DOC</i> [$\text{mg}\cdot\text{l}^{-1}$]	<i>CHL</i> [$\text{mg}\cdot\text{m}^{-3}$]	<i>EC</i> [$\mu\text{S}\cdot\text{cm}^{-1}$]
2015	41.7	13.0	49.3	1 074
2016	37.7	11.5	58.0	1 062
2017	31.4	16.2	62.0	1 069
2018	36.9	12.6	59.9	1 068
2019	38.1	12.2	58.5	1 060
2020	37.3	13.7	60.1	1 064
2021	36.4	13.2	57.6	1 059
2022	37.6	28.9	36.2	1 108

Source: own studies.

Mean *EC* values varied from 1,050 to 1,100 $\mu\text{S}\cdot\text{cm}^{-1}$ except in 2022 when the mean *EC* values were higher than 1,100 $\mu\text{S}\cdot\text{cm}^{-1}$ as well as four times in other years (9 August 2017, 10 September 2018, 22 June 2019 and 1 July 2020). For dates with high *EC* mean values, high spatial variability was also observed, except in 2022 (Fig. 5). The highest yearly values of *EC* (1,108 $\mu\text{S}\cdot\text{cm}^{-1}$) was observed in 2022 and the lowest (1,059 $\mu\text{S}\cdot\text{cm}^{-1}$) in 2021. This result shows low variability in the mean values of *EC* (both yearly and between all images) simultaneously with the high spatial variability indicated by the bars in Figure 2.

Satellite based water quality parameters were validated against 20 ground truth samples measured in 2021 and 2022. Water

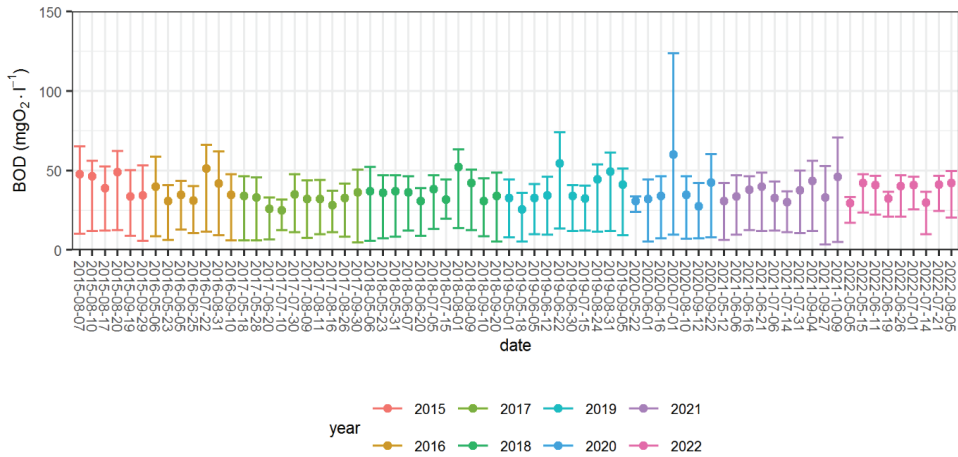


FIGURE 2. Temporal changes in biological oxygen demand (*BOD*) based on all cloud-free pixels within Głuszyńskie Lake for 70 Sentinel-2 images. The dots show mean values, the bars show 5% and 95% quantiles

Source: own studies.

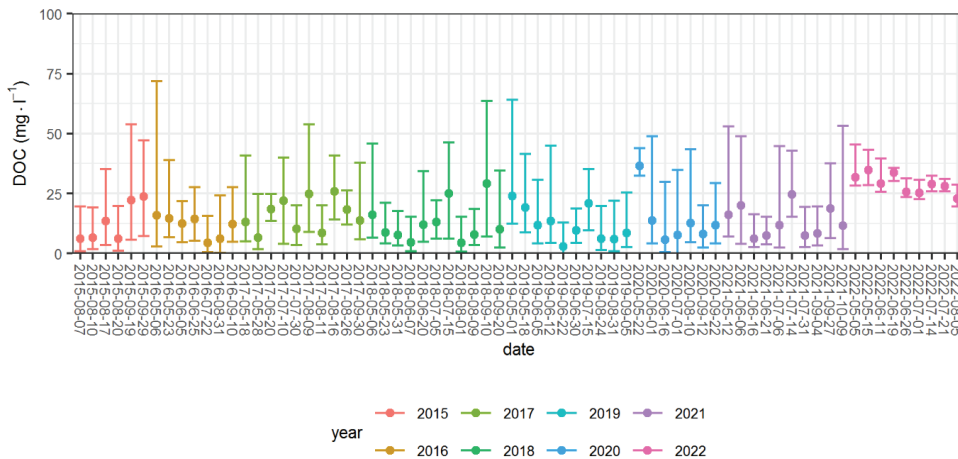


FIGURE 3. Temporal changes in dissolved organic carbon (*DOC*) based on all cloud-free pixels within Głuszyńskie Lake for 70 Sentinel-2 images. The dots show mean values, the bars show 5% and 95% quantiles

Source: own studies.

quality parameters calculated based on satellite images were averaged for neighbouring pixels (3×3 px) before further

comparison. Satellite based water quality parameters would not correspond quantitatively to ground truth data (Fig. 6). However,

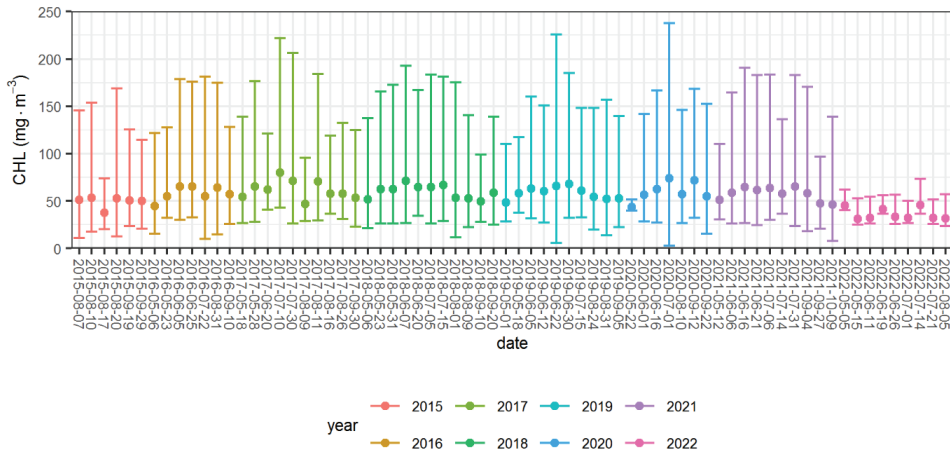


FIGURE 4. Temporal changes of chlorophyll concentration (*CHL*) based on all cloud-free pixels within Głuszyńskie Lake for 70 Sentinel-2 images. The dots show mean values, the bars show 5% and 95% quantiles

Source: own studies.

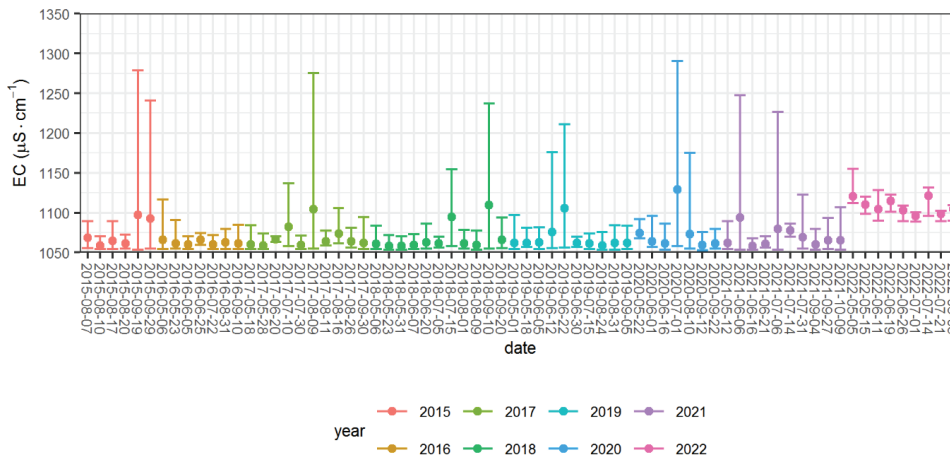


FIGURE 5. Temporal changes in electrical conductivity (*EC*) based on all cloud-free pixels within Głuszyńskie Lake for 70 Sentinel-2 images. The dots show mean values, the bars show 5% and 95% quantiles

Source: own studies.

for *BOD*, *CHL* and *DOC*, a statistically significant ($p < 0.01$) relationship was observed

CHL) with an R^2 of 0.77 (for *CHL* and *DOC*) and 0.79 (for *BOD*). For *EC* the relationship was quadratic, but the R^2 of 0.45 shows that

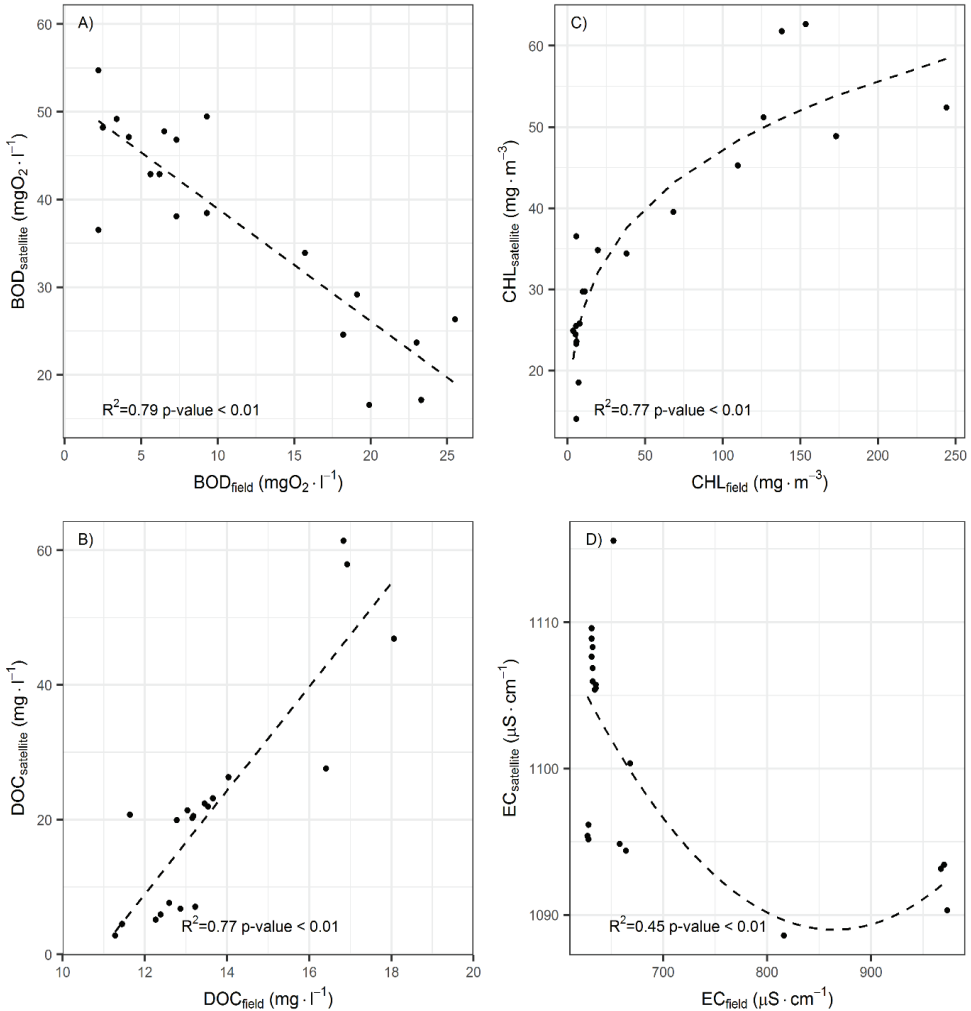


FIGURE 6. Relationships between the models based on satellite images and measurements based on filled measurements for: *BOD* – linear relationship (A); *DOC* – linear relationship (B); *CHL* – power relationship (C) and *EC* – quadratic relationship (D)

Source: own studies.

relationship for this parameter was weaker than for the other.

Additionally, based on data from the nearest meteorological station (Kołó-Radoszewice, operated by the Institute of Meteorology and Water Management –

National Research Institute – IMGW-PIB), we analysed the influence of meteorological elements (temperature, perception and insolation) on water quality parameters on a monthly scale (Table 2). Only for *BOD* and *DOC* did we observe a significant ($p < 0.05$)

TABLE 2. Relationship (and its p value) between the average monthly values of water quality parameters and meteorological elements for Głuszyńskie Lake

	Temperature		Precipitation		Insolation	
	relation	p	relation	p	relation	p
<i>BOD</i>	positive	< 0.05	negative	0.11	positive	0.33
<i>CHL</i>	positive	0.11	positive	0.48	positive	0.61
<i>DOC</i>	negative	< 0.05	positive	0.48	negative	0.11
<i>EC</i>	negative	0.98	negative	0.34	negative	0.66

Source: own studies.

relation with temperature, positive for *BOD* and negative for *DOC*.

Conclusions

This paper shows the results of long-term (since 2015) water quality monitoring of Głuszyńskie Lake using freely available Sentinel-2 data. The strong relationship ($R^2 > 0.75$) between the estimated parameters (*BOD*, *DOC*, *CHL*) and the ground truth data shows its potential qualitative temporal and spatial distribution monitoring to these parameters. Yearly mean values of the parameters show low variation, but the application of remotely sensed data allows the detection of peak values (if they occur close to a satellite overpass without cloud cover) and the spatial distribution of those parameters, which is practically impossible with the use of traditional monitoring methods.

Funding

The study was co-financed by the research and development project, RPKP.01.03.01-04-0001/19, co-financed by the European Regional Development Fund,

under submeasure RPKP.01.03.01. Support for research and development processes in academic enterprises, the Regional Operational Program of the Kujawsko-Pomorskie Voivodeship for 2014–2020, “*Działania o charakterze badawczo-rozwojowym nad stworzeniem innowacji produktowej i procesowej w skali światowej związanej z wykorzystaniem bezzałogowego statku powietrznego, z zestawem dedykowanych urządzeń optyczno-analitycznych, do monitorowania szeregu elementów przyrody ożywionej i nieożywionej* [Research and development activities on the creation of a product and process innovation on a global scale related to the use of an unmanned aerial vehicle, with a set of dedicated optical-analytical devices for monitoring a number of elements of animate and inanimate nature]”, led by Air-Concept Ltd Co.

Acknowledgements

The meteorological data were made available by the Institute of Meteorology and Water Management – National Research Institute (IMGW-PIB) in Poland.

References

- Abdelmalik, K. W. (2018). Role of statistical remote sensing for inland water quality parameters prediction. *The Egyptian Journal of Remote Sensing and Space Science*, 21 (2), 193–200.
- Brando, V. E. & Dekker, A. G. (2003). Satellite hyperspectral remote sensing for estimating estuarine and coastal water quality. *IEEE Transactions on Geoscience and Remote Sensing*, 41 (6), 1378–1387.
- Duan, W., He, B., Takara, K., Luo, P., Nover, D., Sahu, N. & Yamashiki, Y. (2013a).

- Spatiotemporal evaluation of water quality incidents in Japan between 1996 and 2007. *Chemosphere*, 93 (6), 946–953.
- Duan, W., Takara, K., He, B., Luo, P., Nover, D. & Yamashiki, Y. (2013b). Spatial and temporal trends in estimates of nutrient and suspended sediment loads in the Ishikari River, Japan, 1985 to 2010. *Science of the Total Environment*, 461, 499–508.
- Gholizadeh, M. H., Melesse, A. M. & Reddi, L. (2016). A comprehensive review on water quality parameters estimation using remote sensing techniques. *Sensors*, 16 (8), 1298.
- Giardino, C., Bresciani, M., Cazzaniga, I., Schenk, K., Rieger, P., Braga, F., Matta, E. & Brando, V. E. (2014). Evaluation of multi-resolution satellite sensors for assessing water quality and bottom depth of Lake Garda. *Sensors*, 14 (12), 24116–24131.
- Gitelson, A. A., Dall’Olmo, G., Moses, W., Rundquist, D. C., Barrow, T., Fisher, T. R., Gurlin, D. & Holz, J. (2008). A simple semi-analytical model for remote estimation of chlorophyll-a in turbid waters: Validation. *Remote Sensing of Environment*, 112 (9), 3582–3593.
- Hadjimitsis, D. G. & Clayton, C. (2009). Assessment of temporal variations of water quality in inland water bodies using atmospheric corrected satellite remotely sensed image data. *Environmental Monitoring and Assessment*, 159 (1), 281–292.
- International Organization for Standardization [ISO] (1999). *Water quality. Guidelines for the determination of total organic carbon (TOC) and dissolved organic carbon (DOC)* (ISO 8245). Geneva.
- Kloiber, S. M., Brezonik, P. L., Olmanson, L. G. & Bauer, M. E. (2002). A procedure for regional lake water clarity assessment using Landsat multispectral data. *Remote Sensing of Environment*, 82 (1), 38–47.
- Mancino, G., Nolè, A., Urbano, V., Amato, M. & Ferrara, A. (2009). Assessing water quality by remote sensing in small lakes: the case study of Monticchio lakes in southern Italy. *iForest-Biogeosciences and Forestry*, 2 (4), 154.
- Morel, A. & Prieur, L. (1977). Analysis of variations in ocean color I. *Limnology and Oceanography*, 22 (4), 709–722.
- Osińska-Skotak, K. (2010). Metodyka wykorzystania super- i hiperspektralnych danych satelitarnych w analizie jakości wód śródlądowych [Methodology of using super- and hyperspectral satellite data for inland water quality analysis]. *Prace Naukowe Politechniki Warszawskiej. Geodezja*, 47, 3–153.
- Polski Komitet Normalizacyjny [PKN] (2002). *Jakość wody. Pomiar parametrów biochemicznych. Spektrometryczne oznaczenie stężenia chlorofilu a* (PN-ISO 10260). Warszawa.
- Potes, M., Rodrigues, G., Penha, A. M., Novais, M. H., Costa, M. J., Salgado, R. & Morais, M. M. (2018). Use of Sentinel 2 – MSI for water quality monitoring at Alqueva reservoir, Portugal. *Proceedings of the International Association of Hydrological Sciences*, 380, 73–79.
- R Core Team (2020). R: A language and environment for statistical computing. R Foundation for Statistical Computing, Vienna. Retrieved from: <http://www.r-project.org/index.html> [accessed: 28.11.2022].
- Ranghetti, L., Boschetti, M., Nutini, F. & Busetto, L. (2020). “sen2r”: an R toolbox for automatically downloading and preprocessing Sentinel-2 satellite data. *Computers & Geosciences*, 139, 104473.
- Ritchie, J. C., Zimba, P. V. & Everitt, J. H. (2003). Remote sensing techniques to assess water quality. *Photogrammetric Engineering & Remote Sensing*, 69 (6), 695–704.
- Słapińska, M., Berezowski, T., Frąk, M. & Chormański, J. (2016). Retrieval of water quality algorithms from airborne HySpex camera for oxbow lakes in north-eastern Poland. In *EGU General Assembly 2016*, 17-22 April 2016 Vienna. Book of abstracts. Vol. 18, EPSC2016-14167.
- Ścisłowski, Ł., Państwowe Gospodarstwo Wodne Wody Polskie – KZGW, Wydział SIGW (10.03.2022). Wody Polskie – Baza WMS. ver. 1.0.1. QGIS Python Plugins Repository. Retrieved from: https://github.com/LScislawski/Wody_Polskie_Baza_WMS [accessed: 28.11.2022].
- U.S. Environmental Protection Agency [EPA] (1983). Total Organic Carbon. Method 415.1. (Combustion or Oxidation). In *Methods*

for the Chemical Analysis of Water and Wastes (EPA/600/4-79/020). Cincinnati, OH. Retrieved from: https://www.wbdg.org/FFC/EPA/EPACRIT/epa600_4_79_020.pdf [accessed: 28.11.2022].

Summary

Long-term water quality monitoring using Sentinel-2 data, Głuszyńskie Lake case study. This study shows the results of long-term inland water monitoring using Sentinel-2 data for Głuszyńskie Lake in the years 2015–2022. Four water quality

parameters: biological oxygen demand (*BOD*), dissolved organic carbon (*DOC*), chlorophyll concentration (*CHL*) and electrical conductivity (*EC*) were calculated according to formulas found in the literature. The results were validated based on measurements conducted in 2021 and 2022, where for *BOD*, *DOC* and *CHL* high determination coefficients (0.77 and 0.79) were observed, and the *EC* determination coefficient was equal to 0.45. The results show that empirical formulas can be used for qualitative analyses of inland water quality, while for quantitative analyses more extensive field work needs to be performed.

Instruction for Authors

The journal publishes in English languages, peer-reviewed original research, critical reviews and short communications, which have not been and will not be published elsewhere in substantially the same form. Author of an article is required to transfer the copyright to the journal publisher, however authors retain significant rights to use and share their own published papers. The published papers are available under the terms of the principles of Open Access Creative Commons CC BY-NC license. The submitting author must agree to pay the publication charge (see Charges).

The author of submitted materials (e.g. text, figures, tables etc.) is obligated to restricts the publishing rights. All contributors who do not meet the criteria for authorship should be listed in an Acknowledgements section of the manuscript. Authors should, therefore, add a statement on the type of assistance, if any, received from the sponsor or the sponsor's representative and include the names of any person who provided technical help, writing assistance, editorial support or any type of participation in writing the manuscript.

Uniform requirements for manuscripts

The manuscript should be submitted by the Open Journal System (OJS) at <https://srees.sggw.edu.pl/about/submissions>. All figures and tables should be placed near their reference in the main text and additionally sent in a form of data files (e.g. Excel, Visio, Adobe Illustrator, Adobe Photoshop, CorelDRAW). Figures are printed in black and white on paper version of the journal (color printing is combined with an additional fee calculated on a case-by-case basis), while on the website are published in color.

The size of the manuscript should be limited up to 10 pages including overview, summary, references and figures (the manuscript more than 13 pages is unacceptable); Please set the text format in single column with paragraphs (A4 paper format), all margins to 25 mm, use the font Times New Roman, typeface 12 points and line spacing one and half.

The submitted manuscript should include the following parts:

- name and SURNAME of the author(s) – up to 5 authors
- affiliation of the author(s), ORCID Id (optional)
- title of the work
- key words
- abstract (about 500 characters)
- text of the paper divided into: Introduction, Material and Methods, Results and Discussion, Conclusions, References and Summary
- references in APA style are listed fully in alphabetical order according to the last name of the first author and not numbered; please find the details below
- post and mailing address of the corresponding author:

Author's address:

Name, SURNAME

Affiliation

Street, number, postal code, City

Country

e-mail: address@domain

- Plagiarism statement (<https://srees.sggw.edu.pl/copyright>)

Reference formatting

In the Scientific Review Engineering and Environmental Sciences the APA 6th edition style is used.

Detailed information

More information can be found: <https://srees.sggw.edu.pl>

